UNIVERSITY OF TARTU

Faculty of Science and Technology

Institute of Technology

Juri Volodin

MODELING AND EXPERIMENTAL STUDY OF THE BIEFELD-BROWN EFFECT

Bachelor's Thesis (6 EAP)

Supervisors: Prof. Alvo Aabloo

Assoc. Prof. Andreas Kyritsakis

Prof. Vahur Zadin

Tartu 2021

Abstract

Juri Volodin

University of Tartu, Institute of Technology

Modeling and experimental study of the Biefeld-Brown effect

Bachelor's thesis 2021

Supervisors: Prof. Alvo Aabloo, Assoc. Prof. Andreas Kyritsakis, Prof. Vahur Zadin

This work introduces the computational model of the Biefeld-Brown effect, thrust generation in the air-filled asymmetric capacitor due to the ionization process on the smaller electrode, and the transfer of potential energy of electric field into kinetic energy of ionized particles and further momentum transfer to neutral particles via collision mechanism. This phenomenon is numerically simulated and experimentally studied to utilize it for drag reduction purposes in the transportation industry. If thrust is generated tangentially to the surface, it mobilizes the boundary level of air and decreases the drag. This computational model does not consider any drag calculations. The emphasis is on the Biefeld-Brown effect as the first step for further research. The 2D finite element model was created for numerical simulation as the studied system was long enough to neglect the edge effects. Several types of experimental setups were proposed and tested for thrust measurement. The experimental setup for more precise thrust measurement was developed.

Keywords: Biefeld-Brown effect, FEM, corona discharge, electrohydrodynamics, ion thruster, drag reduction

CERCS: P200

Lühikokkuvõte

Biefeld-Brown’i efekti modelleerimine ja eksperimentaalne uurimine

Uurimistöö eesmärgiks on luua Biefeld-Brown´i efekti arvutuslik mudel. Biefeld-Brown’i efekt tekib asümmetrilises õhuga täidetud kondensaatoris, mille väiksema elektroodi läheduses ioniseeruvad õhu osakesed. Tekkinud ioonid hakkavad elektrivälja mõjul liikuma (elektrivälja potentsiaalne energia konverteeritakse liikuvate ioonide kineetiliseks energiaks) ja põrkuvad neutraalsete osakestega, andes edasi impulsi, mille tulemusena tekib tõukejõud. Kirjeldatud nähtust uuritakse töös arvutuslikult ja eksperimentaalselt. Uuritava süsteemi piisav pikkus võimaldab luua 2D lõplike elementide mudeli küljeefekte arvestamata. Tõukejõu mõõtmiseks töötati välja ja viidi läbi mitu erinevat katset, mille tulemusena arendati välja uus katsekorraldus tõukejõu täpsemaks mõõtmiseks. Loodud arvutuslik mudel ei käsitle õhu takistuse arvutusi, vaid keskendub Biefeld-Brown’i efekti enda uurimisele ning on aluseks edasisele teadustööle. Kui nimetatud efekti tekitatud tõukejõudu rakendada pinnaga tangentsiaalselt, paneb see liikuma piirpinnal oleva õhukihi ja vähendab seeläbi õhutakistust – seetõttu saaks uurida Biefeld-Browni’i efekti tõhusust õhu takistuse vähendamisel transpordis.

Märksõnad: Biefeld-Brown’i effect, FEM, koroona lahendus, elektrohüdrodünaamika, takistuse vähendamine

CERCS: P200

Table of Contents

Notations/Abbreviations

Notation/ Abbreviation	Unit	Explanation
BB effect		Biefeld-Brown effect
EHD		Electrohydrodynamics
FEM		Finite element method
E_0	V/m	Breakdown electric field strength of air, $3.31 \cdot 10^6$ V/m
E_S	V/m	Electric field strength on the boundary of the air ionizing electrode
r_0	cm	Radius of an ionizing electrode
ε_0	C /(V·m)	Dielectric permittivity of free space
ε_r	∅	Relative permittivity of the air
μ_E	m^2 /(V·s)	Mobility of charged molecules in the air medium, 1.8×10^{-4} m^2 /(Vs)
ρ_{air}	kg/m^3	Air density
θ	N/kW	Thrust power efficiency
ϕ	N/m^2	The thrust's ratio to the area of the fluid flow
D	m^2/s	Charge diffusion coefficient, 5.3×10^{-5} m^2/s
H	g/m^3	Absolute humidity
T	N	Thrust
p	Pa	Air pressure
$\boldsymbol{E}$	V/m	Electric field strenght
$\boldsymbol{J}$	A/m^2	Electric current density
μ	kg/(m·s)	Dynamic viscosity of a fluid (air), 1.8×10^{-5} kg/(m·s)
ρ	C/m^3	Space charge density

1 Introduction

Electrohydrodynamics (EHD) describes the dynamics of electrically charged fluids. In EHD, ionized particles, their interactions, electric fields, and the surrounding fluid are studied.

The Biefeld-Brown effect is an electrohydrodynamic effect observed in an air-filled capacitor, commonly asymmetric, when a sufficiently high voltage, starting from several kilovolts, is applied on the electrodes of the capacitor. In this case, the electric field strength close to one of the electrodes reaches the dielectric breakdown strength of the air. Thus, air molecules are ionized and directed by the electric field to the other electrode(s). This movement eventually generates thrust in the direction of the positive electrode in a symmetric capacitor. In an asymmetric capacitor, though, the force is directed towards the electrode with smaller curvature and larger radius.

Thorough research and estimations on the viability of the utilization of the BB effect in propulsion were conducted by Wilson in his paper for NASA in 2009 [1]. He investigated and compared known geometries for thrusters that utilize the BB effect. The goal for the technology to be competitive with existing propulsion systems was set. Namely, thrust power efficiency $\theta = 20$ N/kW and thrust effective pressure (the thrust's ratio to the fluid flow's area) $\phi = 20$ N/m^2. In the paper, the goal for $\theta = 20$ N/kW was achieved, but not for ϕ. Therefore, it was concluded that the BB effect does not seem to be applicable in propulsion. Since then, there was no significant improvement in the field. However, a few attempts were made to utilize the Biefeld-Brown effect to decrease air friction [2], [3]. In these articles, it is claimed that EHD thrusters can induce a drag reduction reaching 30%. This thesis will concentrate on understanding the Biefeld-Brown effect and its potential application for drag reduction of moving objects. Although BB thrusters are not suitable for propulsion, several qualities make them very interesting for active airflow control near the surface of a moving body. First of all, they have no moving parts. Secondly, they have rapid response times. Thirdly, they can be miniaturized and installed in large quantities on the surface of a moving object.

1.1 Motivation of the research

1.1.1 Importance of the scientific field

Nowadays, efficient transportation is vital for the functioning of society. It is increasingly important in logistics to attain maximal speeds while decreasing fuel consumption. In dense atmospheres, the aerodynamic drag of a vehicle has a quadratic relationship with its speed. When the running speed reaches 300 km/h, the aerodynamic drag can account for more than 80% of the total drag. For increasing maximal speed, a new concept was proposed, namely the Hyperloop. It is a system of vacuum-sealed tubes and a vehicle that electromagnetically levitates at high speed along the tube [4], [5]. While it is an ambitious project with no doubt in its future value in transportation, it is still difficult and expensive to implement within the existing transportation infrastructure.

1.1.2 The state of the art

An alternative approach would be to decrease the air friction utilizing the BB-effect on the surface of a vehicle, e.g. an aircraft or a rocket. This approach can increase the maximal speed of a vehicle as well as potentially decrease fuel consumption. Moreover, this topic has not yet been studied very deeply. As to the author's best knowledge, there were only few publications about the utilization of corona discharge to decrease the drag [2], [3].

In recent years, another type of air ionization device is extensively studied for drag reduction purposes, the so-called dielectric barrier discharge plasma actuator [6]–[9]. It is an alternating current plasma generating device, with one of the electrodes covered by a dielectric material. This type of thruster can work with lower voltages.

However, it is much more challenging to control this type of thrust by a magnetic field, as the generated airflow contains regions of both positive and negative ions. In contrast to that, the DC corona discharge is more suitable for manipulation with magnetic fields. Matsoukas and Ahmed [10] were able to increase the thrust of an EHD thruster by several percent by simply placing a permanent magnet close to the system of electrodes. No more studies were conducted considering the influence of magnetic fields on the corona discharge drag reduction efficiency and control.

1.1.3 Beyond the state of the art

In future research, it is desired to find the most efficient arrangement of electrodes and magnets on the surface for this system to be applicable in the transportation industry. Also, appropriate

materials have to be chosen for the electrodes and the magnets to be applicable in this area. To achieve this goal, it would be important to create and experimentally validate a precise magneto-electrohydrodynamic model coupled with a drag reduction calculation.

1.1.4 The gap for improvement

Building this type of model is challenging as it combines many different phenomena, such as fluid dynamics, electromagnetics and different drag calculations. So, it is reasonable to subdivide it into several models and start with a model predicting the thrust dependence on the voltage. This model should also describe the physical behavior of ionized air and its interaction with neutral air, predict velocities and volume forces for their implementation in the next models. For this reason, several aims have been set to accomplish in this thesis.

1.2 Objectives

This thesis will concentrate on the following objectives:

- Increase understanding of the Biefeld-Brown effect and clarify the origin of the thrust force as well as gain initial information about the safety of employment of the BB effect.
- Create a model of the Biefeld-Brown effect utilizing the finite element method (FEM) in the software package for equation-based multiphysics modeling COMSOL Multiphysics® [11].
- Create an experimental setup and conduct experiments to validate the simulation model.
- Propose further steps of research for creating a drag reduction system for moving objects.

2 Overview of Beifeld-Brown effect

2.1 Literature review on electrohydrodynamics and the Biefeld-Brown effect

Niccolo Cabeo firstly studied EHD effects in 1629. He noticed that sawdust particles attract to electrified bodies and are repelled after touching [12]. However, Cabeo was not able to explain the true nature of the effect. Thus the discovery of EHD can be attributed to Francis Hauksbee in 1709, who recorded that an electrically charged tube generates a weak wind [13].

The Biefeld-Brown effect was discovered around 100 years ago by Paul Biefeld and Thomas Townsend Brown and was falsely connected to antigravity properties of high magnitude electric fields. However, this connection appeared to be undoubtedly wrong, and this way diverted the attention of many serious-minded researchers from this question for some time. In 1960 Brown was granted another patent, titled *"Electrokinetic Apparatus,"* where he introduced the concept of dielectric fluid movement and disconfirmed any electro-gravity explanation [14].

De Seversky reproduced Brown experiments with an asymmetrical capacitor for propulsion and created a new term "Ionocraft." The results of his work were published in *Popular Mechanics*

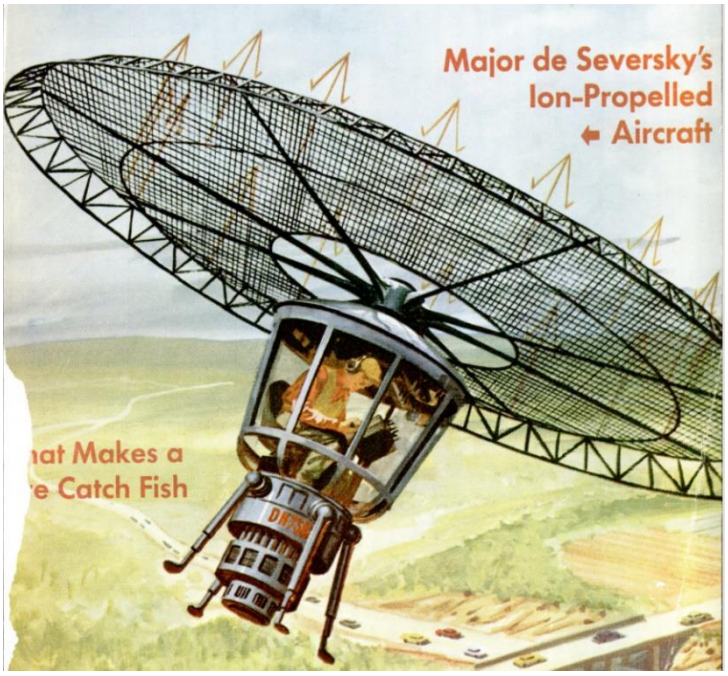

Fig. 1 Futuristic illustration from *Popular Mechanics* magazine [15].

magazine in 1964 [15]. He prognosed that ionocraft will be able to lift significant weights. Unfortunately, he couldn't create devices that could lift weights larger than hundred grams.

First, theoretical work on the topic by Cheng was published in 1962. Cheng made three essential conclusions about EHD propulsion. Firstly, he concluded that a more significant thrust could be achieved more economically by increasing the electrode area than operating in the abnormal glow region. Higher thrust is observed in an abnormal glow region, but it is accompanied by larger power consumption. Secondly, for the same thrust, the discharge current density of the corona and consequently the power consumption may be decreased by using gases with larger ion mass and smaller saturation ionization constants. Hence, smaller ion mobility μ results in reduced power consumption for a particular thrust. Lastly, it was concluded that the thrust and the discharge current increase with the square of the gas pressure [16].

A second theoretical paper by Christenson and Moller was published in 1967 [17]. In their work, they employed for the first time the Navier-Stokes equation for their 1D model of an EHD thruster and validated it with experimental results. The experimental setup consisted of sharp-pointed aluminum rods mounted on plexiglass for the emitter electrode and collecting electrode, which consisted of concentric aluminum rings. The experimental thruster efficiency was about twice smaller than predicted by their model. Christenson and Moller concluded that approximately 90% of the input energy was lost in the form of heat and therefore, for practical applications it is necessary to reduce the ion mobility μ of air molecules by at least 2 orders of magnitude, which will lead to a competitive efficiency level of approximately 30%. However, it is important to mention that this conclusion was made based on the particular geometry of the system, thus cannot be directly applied to other more improved geometries.

In the same period, particularly in 1961, there was another similar work by Robinson [18]. He mentioned the relatively low conversion rate of the EHD system and some production of ozone as well as a tiny amount of nitrogen dioxide during the negative corona. Fortunately, the positive corona is more efficient for propulsion and, at the same time, produces significantly less ozone. Bondar and Bastien [19] showed in their work that energy conversion efficiency increases up to 7.5% if the thruster operates with a flow velocity of 50 m/s. In 1988, Robert Talley was the first to conduct experiments with the BB effect in a vacuum chamber [20]. Talley did numerous experiments with gas pressures reaching down to $1.33 \cdot 10^{-4}$ Pa. He used a torsion pendulum with asymmetrical electrodes placed in a manner that the generated thrust caused the pendulum to rotate. He reported that no significant force was observed in a vacuum. Talley explained the small movements of the device by the interaction of electrodes with the vacuum chamber. Thus, it once again suggests that the origin of the force is the electrostatic interaction

between charged air molecules and electrodes and the consequent transfer of momentum to neutral molecules. After Talley's report, there was a decline in research on the topic.

In recent decades, interest in the Biefeld-Brown effect recommenced due to its potential application in propulsion technologies [1], [10], [21]–[24].

2.2 Biefeld-Brown effect simple theoretical model

Before starting with numerical simulations of the BB effect, it is useful to acquire an intuitive understanding by deriving a few simple formulas for the thrust T and power efficiency θ. First of all, the mechanism of generation of ionized particles appears to be the corona discharge in the vicinity of the charged electrode. It is considered to happen through photoionization of an air molecule and consequent avalanche in the direction of a positively charged electrode [25]. In this thesis, only the positive corona discharge is addressed because of its ability to generate

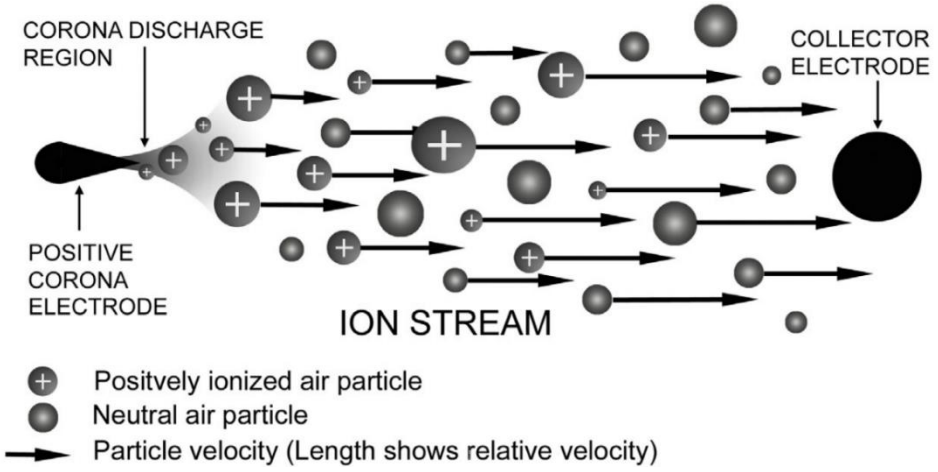

Fig. 2 Thrust creation in asymmetric capacitor [24].

a larger thrust than a negative corona [26]. The space close to a charged electrode, where particles are ionized, is generally called the ionization region or the corona discharge region. The rest of the interelectrode region, where the directed movement of charged particles as well as collisions with neutral air molecules take place, is called the drifting region.

Christenson and Moller [1], [17] showed that the equation for thrust T can be simply derived by assuming that the electric field is uniform in the ionization region, which is certainly not true, but they used it as an approximation for a simple model derivation. There is now production of ions outside the ionization region; hence the product of ion density n_j and flow cross-section A is constant in the drifting region. A single ion experiences an electrostatic force T_j is

$$T_j = eE \tag{1}$$

where E is the electric field strength in the drifting region, and e is the unit charge. The total force T on all ions is then

$$T = NT_j = NeE \tag{2}$$

where N is the total number of ionized molecules in the flow and equals to

$$N = n_j Ad, \tag{3}$$

where d is the distance between electrodes, A is a cross-section of flow. The current can be expressed as

$$I = v_j e n_j A, \tag{4}$$

where v_j is the average ion velocity, given by

$$v_j = \mu E \tag{5}$$

in which μ is the ion mobility. This way, the total thrust is

$$T = NeE = n_j AdeE = \frac{(v_j e n_j A)dE}{\mu E} = \frac{Id}{\mu} \tag{6}$$

The last equation clarifies that the thrust is associated with the attraction of ions' flow to the cathode and its repulsion from the anode.

Now it is possible to derive the thrust power efficiency θ

$$\theta = \frac{T}{P} = \frac{Id}{\mu IV} = \frac{1}{E\mu} \tag{7}$$

Equation (7) shows a trade-off between maximal thrust and power efficiency, because stronger electric field generates more significant thrust while decreasing power efficiency. An alternative approach is to decrease the ion mobility μ, which slightly depends on the humidity of the air [27]. Christenson and Moller theorize that pulsing of the electric field could potentially decrease the effective mobility, but have no evidence of accomplishing that experimentally [17].

2.3 Environmental and safety concerns

It is vital to estimate the environmental and health impact of the Biefeld-Brown effect before striving to apply it. Nitrogen oxides and ozone can be generated as a consequence of the

Biefeld-Brown effect device operation. Robinson was the first who raised the concern about ozone and nitrogen oxides formation by the BB effect [18]. A concentration of ozone of 0.1 ppm is commonly accepted as the maximum allowable concentration for long periods of exposure [18]. Robinson in his paper mentions that a thruster, which operates with negative corona near sparkover, generates 0.8 ppm of ozone. The author suggests using thrusters in parallel to reduce ozone formation. It is also added that the amount of nitrogen oxides is significantly smaller, though the particular number is not given in the paper. Fortunately, the positive corona regime is more efficient for propulsion and drag reduction purposes and generates much less ozone, which is also beneficial. However, even the negative corona regime would be appropriate and ecologically sustainable for outside usage, since the half-life time of ozone in still and humid air is approximately 40 minutes. It decreases even more with air movement [28]. Hence, the BB effect can be potentially scaled up without any significant harm to the environment and human health. More detailed mechanisms of ozone and nitrogen oxides formation are described by Pancheshnyi [29]. Finally, the Biefeld-Brown effect operates with high voltages; therefore, standard high voltage safety requirements have to be fulfilled.

3 Methodology of the research

3.1 System description

In this thesis, a simple system of electrodes was simulated utilizing Comsol Multiphysics 5.5, and then a prototype was built to experimentally verify the validity of the simulated physics. The system consisted of two electrodes of different sizes: a large aluminum cathode and a small anode made from other metals (copper, tin, brass). The parameters of the electrodes are given in Table 1.

In the simulated system, the volume between two electrodes can be divided into two regions: the region close to the corona electrode, where the ionization occurs, and the drifting region. The drifting region comprises of all the other space between the electrodes where ionized molecules move in the electric field generated by the two electrodes, collide with neutral particles and transfer the momentum that they previously acquired from electrostatic

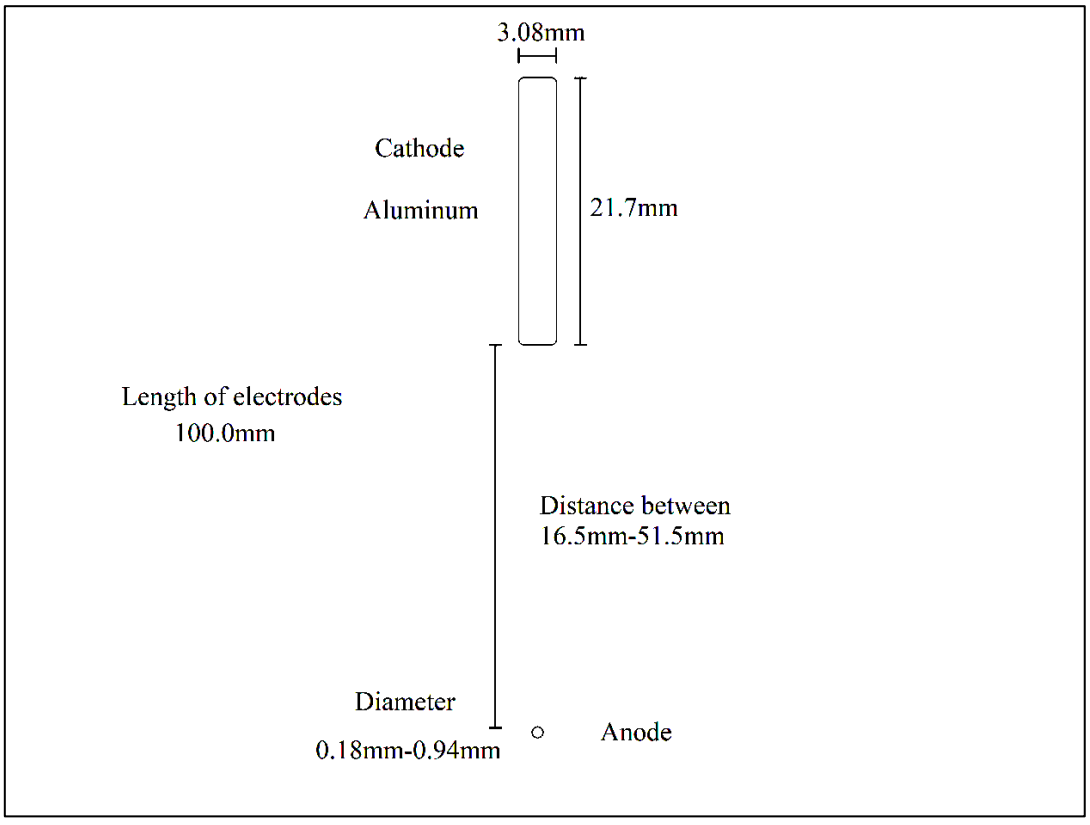

Fig. 3 Geometry of the studied system.

interactions with the electrodes [30]. This way, the potential energy of the electric field is partly transferred into the kinetic energy of airflow.

Parameter	Value
Length of electrodes	100.0 mm
Distance between electrodes	16.5 mm, 31 mm, 51.5 mm
Cathode metal	Aluminum
Cathode width	3.08 mm
Cathode height	21.7 mm
Cathode polarity	Grounded
Anode metal	Brass, copper, tin
Anode diameter	0.18mm, 0.47mm, 0.48mm, 0.52mm, 0.94mm
Anode polarity	Positive

Table 1 Parameters of studied system.

3.2 Electric Field

In order to calculate the electric field $\boldsymbol{E}$ in the air-filled domain we can take the gradient of the electrostatic potential V

$$\boldsymbol{E} = -\boldsymbol{\nabla} V. \tag{8}$$

The electric potential V can be calculated by solving Poisson's equation

$$\nabla^2 V = \frac{\rho}{\varepsilon_0 \varepsilon_r}, \tag{9}$$

where ρ is the space charge density, ε_0 is the dielectric permittivity of free space and ε_r is the relative permittivity of the air. Eq. (9) is solved with the Dirichlet boundary conditions $V = 0$ at the cathode and $V = V_0$ at the anode, where V_0 is the applied voltage.

3.3 Electric current flow

Three processes contribute to the electric current flow in the system: conduction through the motion of ions relative to the airflow, convection (transport of charges with the airflow), and diffusion of charges from regions with larger volume charge density ρ to regions with lower ρ [30]. Conduction is given by $\mu_E \boldsymbol{E}\rho$, where μ_E is the mobility of charged molecules in the air medium. The convection process here is the product of the velocity vector of the airflow $\boldsymbol{U}$ and the space charge density ρ. Diffusion is motivated by the difference of volume charge densities, so it is given by $-D\nabla\rho$, where D is the diffusion coefficient of ions. Combining these three terms together yields the total electric current density

$$\boldsymbol{J} = \mu_E \boldsymbol{E}\rho + \rho\boldsymbol{U} - D\boldsymbol{\nabla}\rho. \tag{10}$$

Assuming that there is no ion generation in the drifting zone, $\boldsymbol{J}$ obeys the continuity equation

$$\boldsymbol{\nabla} \cdot \boldsymbol{J} = 0 \tag{11}$$

3.4 Fluid flow

The fluid flow in the system is solved by assuming laminar flow conditions. As such, we compute the velocity and pressure fields for the flow of a single-phase fluid. The laminarity of the flow is assessed and described by the Reynolds number. The Reynolds number is the ratio of inertial forces to viscous forces in the fluid. The Reynolds number is defined as

$$N_{\mathrm{Re}} = \frac{\rho v d}{\mu}, \tag{12}$$

where ρ is the density of the fluid, v is the fluid velocity, μ is the dynamic viscosity of the fluid, and d is the characteristic length. This important dimension defines the scale of a physical system [31]. A flow remains laminar as long as the Reynolds number is below a particular critical value. At higher Reynolds numbers, disturbances tend to grow and cause the transition to the turbulence regime. This critical Reynolds number depends on the model [32]. Fluid speeds generated by the thruster do not surpass 5m/s, so the flow is slow enough to make a few assumptions. We can consider the fluid to be incompressible and the flow to be laminar.

The fluid flow behavior described by the pressure and velocity fields is found by solving Navier-Stokes and continuity equations.

3.4.1 Continuity equation

The continuity equation or transport equation, describes the transport of some quantity enforcing its mass conservation. Mathematically, it is described in the following way

$$\frac{\partial \rho_{air}}{\partial t} + \boldsymbol{\nabla} \cdot \boldsymbol{j} = \sigma \,, \tag{13}$$

where ρ_{air} is the volumetric density of the quantity, here let it be the air density, t is time, $\boldsymbol{j}$ is the flux of the quantity and σ is the generation of the quantity per unit time per unit volume. In case of quantities that cannot be created or destroyed, such as mass, σ is equal to zero. So, the equation takes a simpler form

$$\frac{\partial \rho_{air}}{\partial t} + \boldsymbol{\nabla} \cdot \boldsymbol{j} = 0 \,. \tag{14}$$

Moreover, if the fluid is incompressible, then it has a constant density, and the equation is even more simplified

$$\boldsymbol{\nabla} \cdot \boldsymbol{j} = 0 \,. \tag{15}$$

This essentially means that no mass or other quantity is generated inside the volume, and the amount entering the volume is equal to the amount leaving it.

As $\boldsymbol{j} = \boldsymbol{U}\rho_{air}$, where $\boldsymbol{U}$ is the velocity of the fluid and ρ_{air} is the density, we can divide both sides of the equation by the density and get the following equation

$$\nabla \cdot \boldsymbol{U} = 0 \,. \tag{16}$$

3.4.2 Navier-Stokes equations

Navier-Stokes equations express the conservation of mass and momentum for Newtonian fluids [33]. They are derived by applying Newton's second law to the motion of fluids and assuming that the stress in the fluids is the sum of the pressure term and a diffusing viscous term (proportional to the gradient of the velocity). Mathematically, Navier-Stokes equations are expressed in the following way

$$\rho_{air}\boldsymbol{U} \cdot \nabla \boldsymbol{U} = -\nabla p + \rho \boldsymbol{E} + \mu \nabla^2 \boldsymbol{U} \,, \tag{17}$$

where the left-hand side of the equation is the acceleration part of Newton's second law, and the right-hand side is the sum of forces existing in the system. ρ_{air} is the fluid density, ρ is the volume charge density from equations (9) and (10), $\boldsymbol{U}$ is the fluid velocity, p is the pressure, E is the electric field strength, and μ is the dynamic viscosity. The first term on the right-hand side of the equation is the pressure gradient forcing the fluid to flow in the direction of the most significant change in pressure. The second is the external electric force. The third term is a diffusion term. In the Navier-Stokes momentum equation, the viscosity operates as diffusion of momentum.

3.5 Simulation procedure

3.5.1 Finite Element Method

In order to numerically solve the above system of partial differential equations, we shall use the finite element method (FEM) [34], [35]. For this, it is necessary to divide the system geometry model into small non-overlapping simple shaped pieces, called subdomains or cells, the set of which is called mesh. For example, linear sections are used in 1D, triangles or quadrilaterals in 2D and tetrahedra or hexahedra in 3D. The points where the corners of neighboring elements intersect are called nodes. The partial differential equations are then solved using this mesh by approximating the solution as a linear combination of piecewise low-order polynomial functions (shape functions) as

$$F(x) = \sum_k F_k N_k(x), \tag{18}$$

where $F(x)$ is the unknown solution, F_k is its values on the k-th node, and N_k is the shape function (or element) associated with the k-th node. The shape functions are non-zero only in the vicinity of their associated node and $N_k(x_n) = \delta_{kn}$, i.e. each shape function is zero in every node except for the one associated with it. Fig. 4 is a schematic illustration of a field, $F(x)$ in 1D, that is approximated using the FEM. In this case, $F(x)$, is a continuous function that is approximated using piecewise linear functions in an element. Utilizing this approximation and the above properties of $N_k(x)$, the differential equation is turned into a (sparse matrix) linear system of algebraic equations, which can then be solved numerically [36].

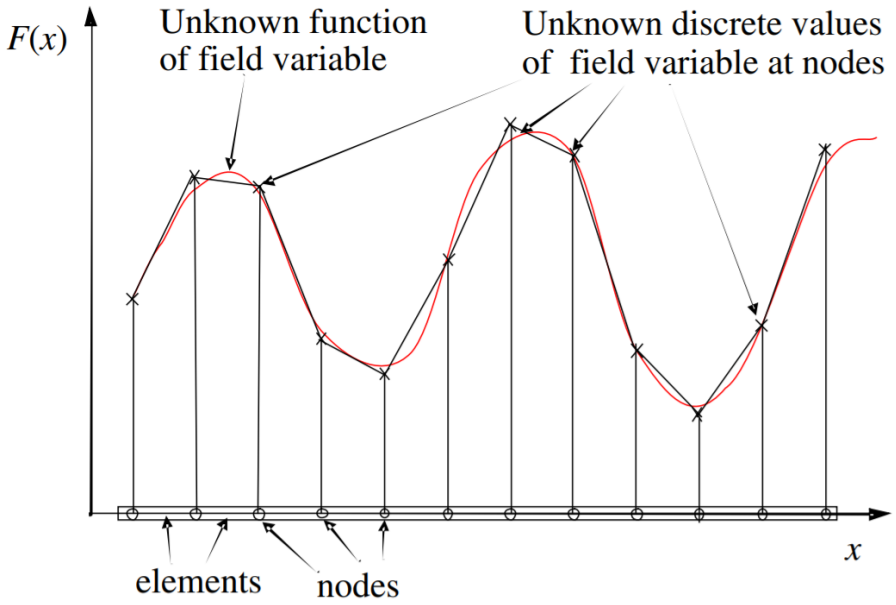

Fig. 4 Finite element approximation for a one-dimensional case. A continuous function is approximated utilizing piecewise linear functions in each element [36].

3.5.2 COMSOL Multiphysics

For modeling the studied system, the COMSOL Multiphysics software was utilized [11]. The *Electrostatics* module was used to solve equations (8) and (9). Electric currents equations (10) and (11) were solved using the *Convection-diffusion* equation module, while the *Laminar flow* module was picked for solving equations (16) and (17).

3.5.3 Simulated geometry and mesh description

Several types of model geometries were simulated numerically. The most promising geometry for the model will be presented here in more detail. It consists of a 0.18 mm in diameter copper anode and an aluminum cathode with the standard dimensions described earlier. The distance between the electrodes is 31.5 mm. It is possible to see in the appendix material from Fig. 26 that the mesh is dense inside the ellipse region in the middle of the model. This was necessary for the adequate calculation of fluid flows in this domain. The total number of elements in the model is 47327.

The remaining part of the model was still necessary for the correct calculation of the electrical potential. In Fig. 5 it is possible to see the larger electrode and the mesh around the small anode. Such a dense mesh was necessary for a precise enough calculation of the space charge density.

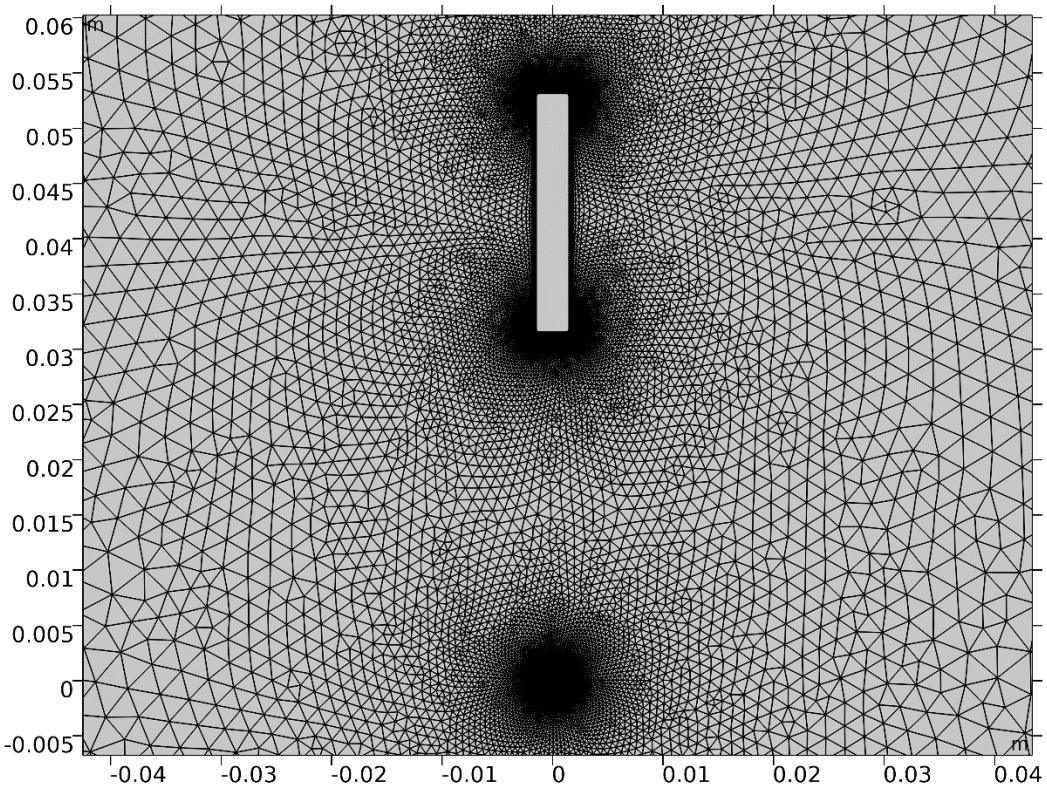

Fig. 5 Mesh close to the electrodes.

In Fig. 27 and Fig. 28 in the appendix, it is possible to see that the mesh on the surface of electrodes changes from triangular to rectangular. This rectangular mesh is called boundary layer mesh. Referring to COMSOL Multiphysics guide: *"A boundary layer mesh is a mesh with an element distribution that is stacked or dense in the direction normal to a boundary. It is created by inserting structured layers of elements along specific boundaries and merging the outer layer with the surrounding structured or unstructured mesh. This type of mesh is useful for many fluid flow applications, especially when coupled to mass and energy transfer, where thin boundary layers need to be resolved "*[32].

3.5.4 Boundary conditions

For solving the set of previously described governing differential equations, boundary conditions have to be imposed. There is a slip wall condition applied on the boundary of the electrodes and the outer walls. It enforces the dot product of the velocity field with the normal vector on the boundary to be zero. The zero pressure point constraint is applied to the bottom corners of the model. For the electrostatics, zero potential is applied on the outer walls of the aluminum electrode, and a varying potential (9kV-29kV) is forced on the smaller electrode. A Dirichlet boundary condition $\rho_0 = 0$ is set for the space charge density on the boundary of the

collector electrode and the outer walls. On the boundary of the small electrode, a boundary value $\rho = \rho_0$ was enforced, with the value of ρ_0 adjusted to satisfy the condition

$$E_S = E_0 \left(1 + \frac{0.586}{r_0^{0.34}}\right) K_H^{-0.2}\,, \tag{19}$$

where E_S is the electric field strength on the boundary of the air ionizing electrode, E_0 the breakdown electric strength of air, r_0 is the radius of the electrode in cm and

$$K_H = 1 + 0.012H^{0.624}\,, \tag{20}$$

where H is the absolute humidity expressed in $\frac{g}{m^3}$. If the voltage applied on the anode is sufficient for corona inception or, in other words, air ionization, then the electric field strength on the surface of the anode is equal to E_S and stays the same even though the applied voltage is increased [25]. An establishment of a dynamic equilibrium explains this phenomenon. The increase of the electrode voltage enlarges the electric field strength and the space charge density in the electrode vicinity. The increased space charge density enhances the screening effect of the electric field. Hence, the electric field strength is limited by the negative feedback mechanism of the space charge density. However, for significantly smaller and larger electrodes, the equation representing E_S is not precise. However, the conditions studied in this thesis are well within the fitting regime.

3.6 Experimental setup design

An experimental setup was built to validate the simulated physics model. The purpose of the setup was to measure the thrust generated by the system of electrodes as a function of voltage and current. Several setups were built to achieve good measurements. For the first attempt the same approach as in existing scientific literature was taken [1], [26], [37]. A stand for electrodes was build from dielectric and put on the scale. When voltage was applied on the electrodes, the created thrust was measured by the scale. In a few papers, the scale was covered by a grounded aluminum foil to screen it from strong electric fields [1], [26]. Fig. 6 illustrates the main idea behind this approach.

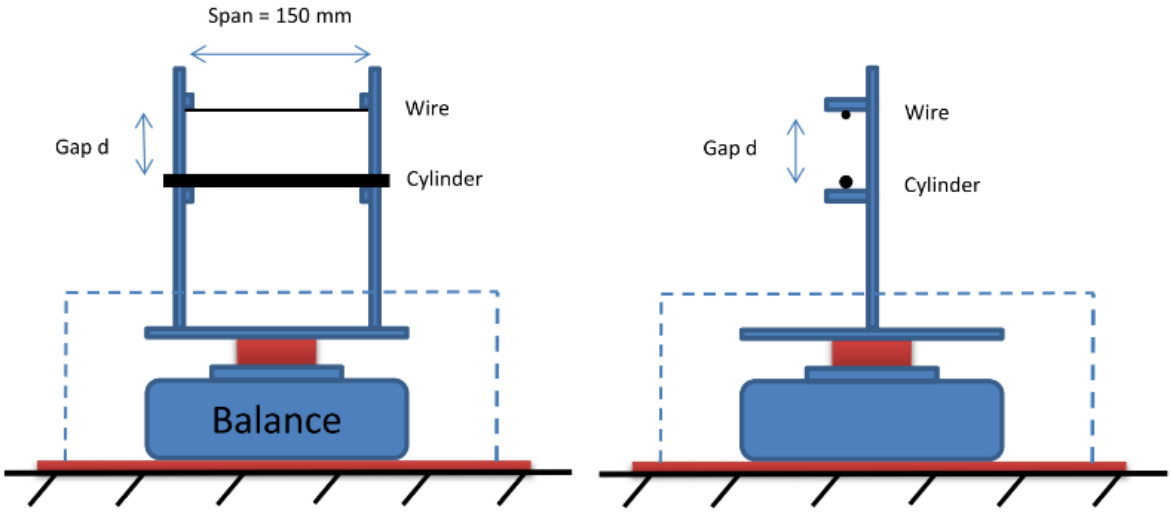

Fig. 6 Setup representing the initial approach [37].

Unfortunately, this solution was not satisfying enough because the aluminum foil used as a faraday cage for the scale also plays a role of a second grounded electrode, increasing or decreasing the thrust depending on the orientation of the system of electrodes. Moreover, it impedes the free movement of the air.

Another experimental setup was created to address this issue. The idea was to move the scale as far as possible from the electrodes. Thus, the test weight on the scale and the system of electrodes were connected by a string situated on two pulleys. The limiting factor for a precise measurement was the friction force of the pulleys and the continuous elongation (creeping) of the string which was made of nylon.

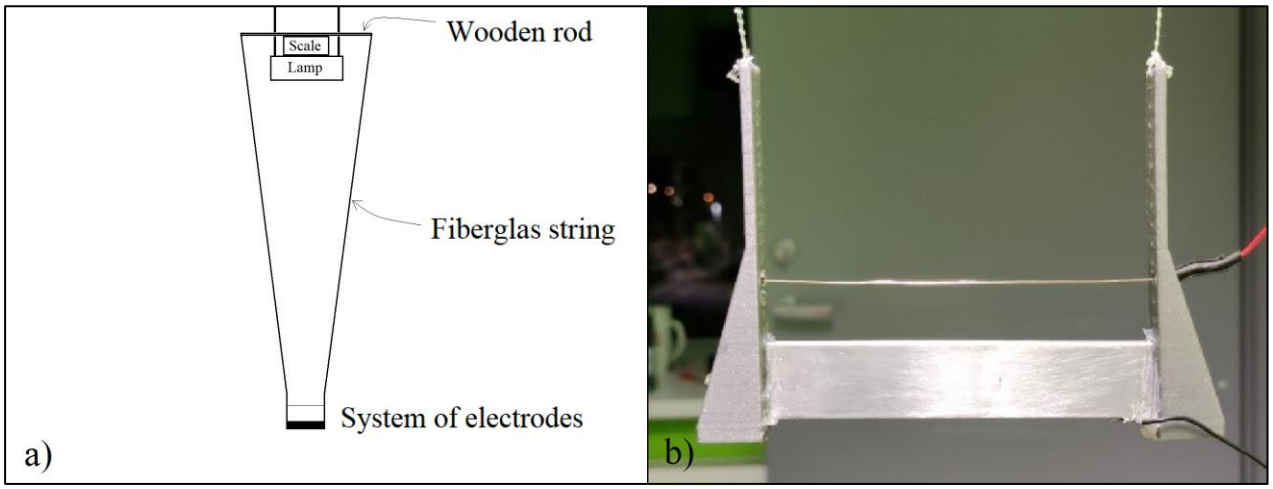

Fig. 7 a) The final experimental setup, b) The system of electrodes

Afterwards, taking the above issues into consideration, the final experimental setup was designed. In this design the scale was placed on a lamp, close to the ceiling. A 30 cm long wooden rod was put on the scale and a string made of glass fiber was used to suspend the plastic construction with the electrodes from the wooden rod. Glass fiber is an appropriate material for the string as it has a larger Young's modulus than nylon. Thus, no creeping effect is observed, while it does not conduct compared to a steel wire. The system of electrodes is suspended far from any conductors, possibly impeding the electric field and obstacles hindering the movement of the air. The distance between the scale and the system of electrodes is approximately 2.3 m. The photo of the electrode arrangement is presented in Fig. 7 b). In this figure the distance between the electrodes is 16.5 mm.

3.6.1 Measurement apparatus and circuitry

The current in the system was measured by taking the voltage drop on a 21.93 kΩ resistor, connected in series with the system of electrodes. The total voltage in the system was measured

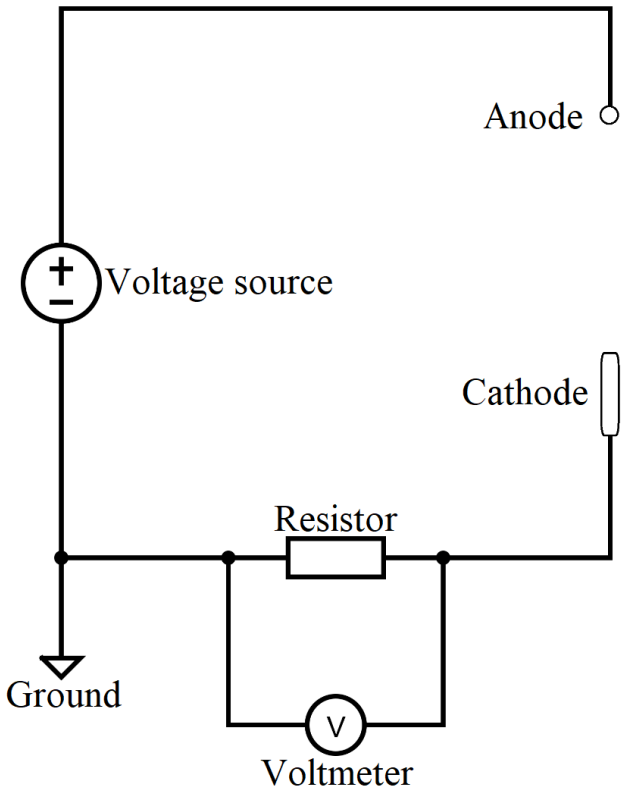

Fig. 8 Experimental setup circuitry.

by the voltage source. The voltage source, as well as the cathode, were grounded. The circuit is represented in Fig. 8.

The characteristics of the utilized measurement equipment are described in Table 2.

Device	Characteristics
DC voltage source	0-30kV, max. output current 0.5mΩ, model name AHVAC30KVR5MABT
Multimeter	Model FLUKE 117 TRUE RMS
Scale	50g max, 0.001g precision
Anemometer	Sefram 9862 hot wire anemometer

Table 2 Characteristics of the measurement equipment.

3.6.2 Measurement procedure

Seven different electrode configurations were tested (different anode metals, distances and anode diameters). For every configuration, voltage was increased from 0 kV to 30 kV or to the breakdown voltage with intervals of 1 kV. When sufficient voltage was applied to the electrodes, the thrust was generated and measured by the scale. After increasing the voltage, sufficient time was given to the system to reach the equilibrium state. The accuracy of the measurement system was checked by putting an exact weight of 0.2220 g on the aluminum electrode and confirming that the scale display shows 0.222 g before every measurement. Therefore, it was verified that the system is put on the scale symmetrically, and no torque is present.

4 Results and discussion

4.1 Simulation results

The length of the simulated model is several times larger than its height and width. So, it was possible to conduct simulations in 2D, significantly decreasing the computational times while keeping a high accuracy, as the edge effects were negligibly small. The most promising simulations were demonstrated by the configuration of electrodes, where the small electrode diameter was 0.18 mm, and the distance between the electrodes was 31.5 mm. The most interesting voltage regime was around 26 kV, as it will be shown in the experimental part. Therefore, the major part of 2D plots will demonstrate the physical behavior of this configuration. Similar plots could be generated for every electrode configuration and voltage regime, though it would lead to a generation of about 600 plots.

4.1.1 Mesh convergence

Simple mesh convergence tests were conducted. It was checked that twice increasing the number of elements in the model changes the thrust values only by 0.1%. However, decreasing the number of elements created more significant differences in the thrust. Hence, the total number of elements in the model was set to be 47327.

4.1.2 Electric potential

The size of the model was chosen in such a way that it did not influence the electric potential. It can be observed in the appendix material in Fig. 29. The boundary condition for the potential on the edges of the air domain was $V = 0$. The distribution of electric potential close to the electrodes is depicted in Fig. 9. Largest values

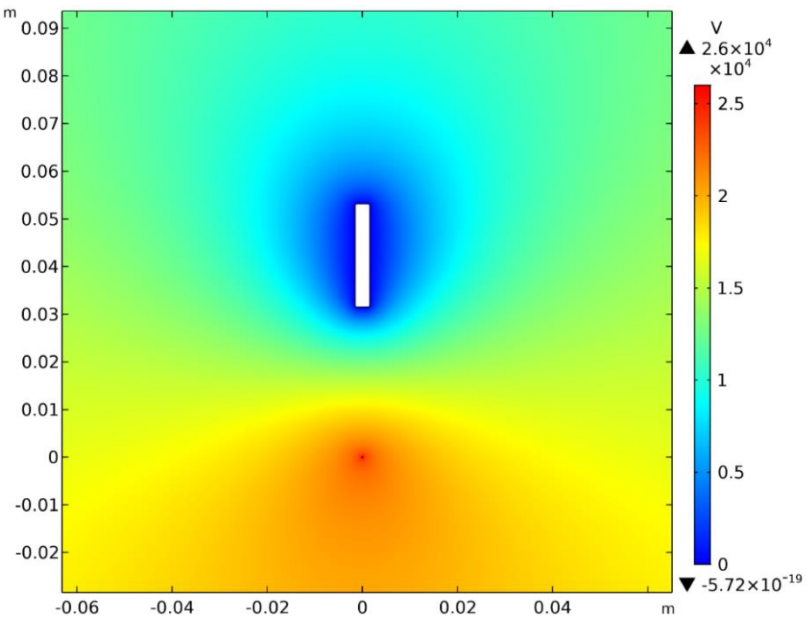

Fig. 9 Calculated electric potential in V (magnified).

of $2.6 \cdot 10^4$ V for electric potential can be observed close to the air ionizing positive anode. The potential on the cathode is equal to zero.

4.1.3 Electric field

Inspecting the direction of the electric field as depicted in Fig. 10, one notes that the electric field between the electrodes is relatively uniform, pointing from the small positive anode

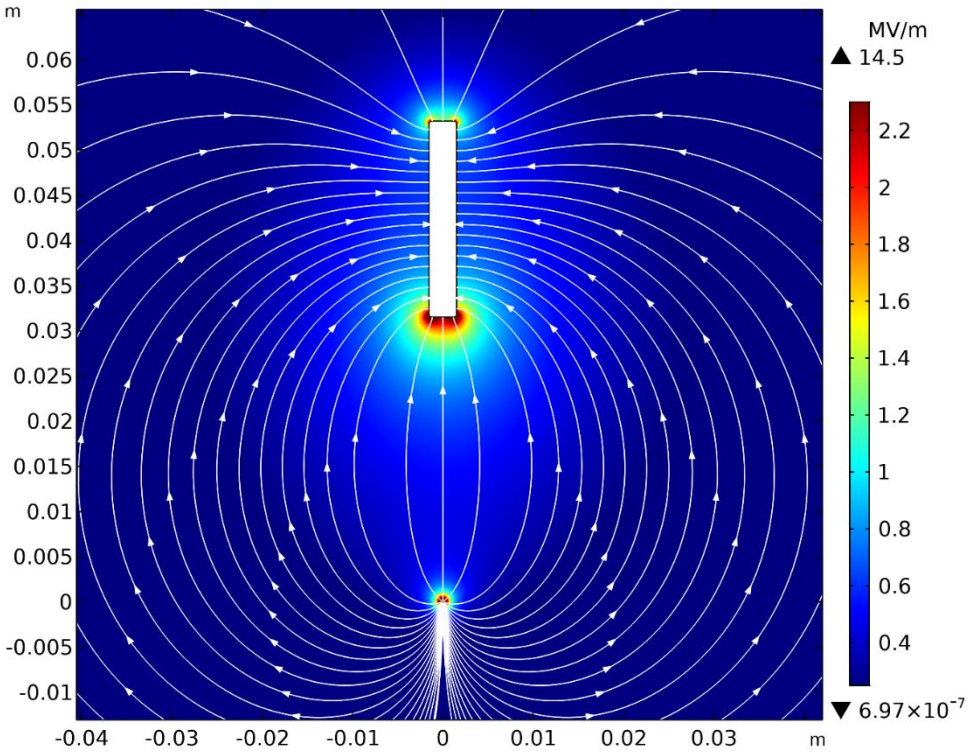

Fig. 10 Calculated electric field in MV/m.

towards the larger cathode, with a magnitude between 0.4 and 1.4 MV/m. The white streamlines show the direction of the electric field. In the appendix Fig. 30 an electric field of 14 MV/m can be observed close to the anode. In this figure the electric field around the anode also seems rather uniform.

4.1.4 Space charge density

The space charge density has a drop-shaped form with a tip pointed towards the larger electrode. The space charge density close to the small electrode is relatively uniform but slightly shifted towards the large electrode. The largest space charge density is located in close vicinity to the anode and reaches magnitudes of $3 \cdot 10^{-4} \ \frac{\mathrm{C}}{\mathrm{m}^3}$.

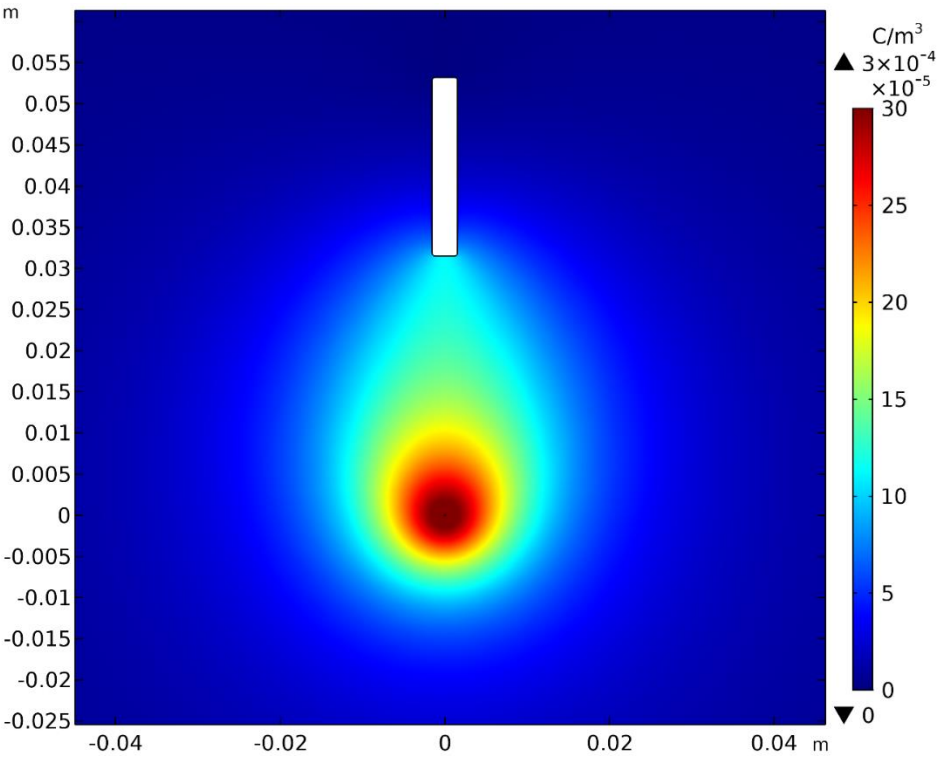

Fig. 11 Calculated space charge density in C/m3.

4.1.5 Velocity of the air

Velocity plots describe the movement of the air. In Fig. 12 the average velocities are around 1.3 m/s. It is possible to see that turbulent regions are formed at a distance of 0.5 m from the system of electrodes. In Fig. 13 it is easier to observe the highest velocities of 2.59 m/s close to the large electrode. In this region, the air was maximally accelerated by the capacitor, but has not yet started losing the momentum due to the friction forces.

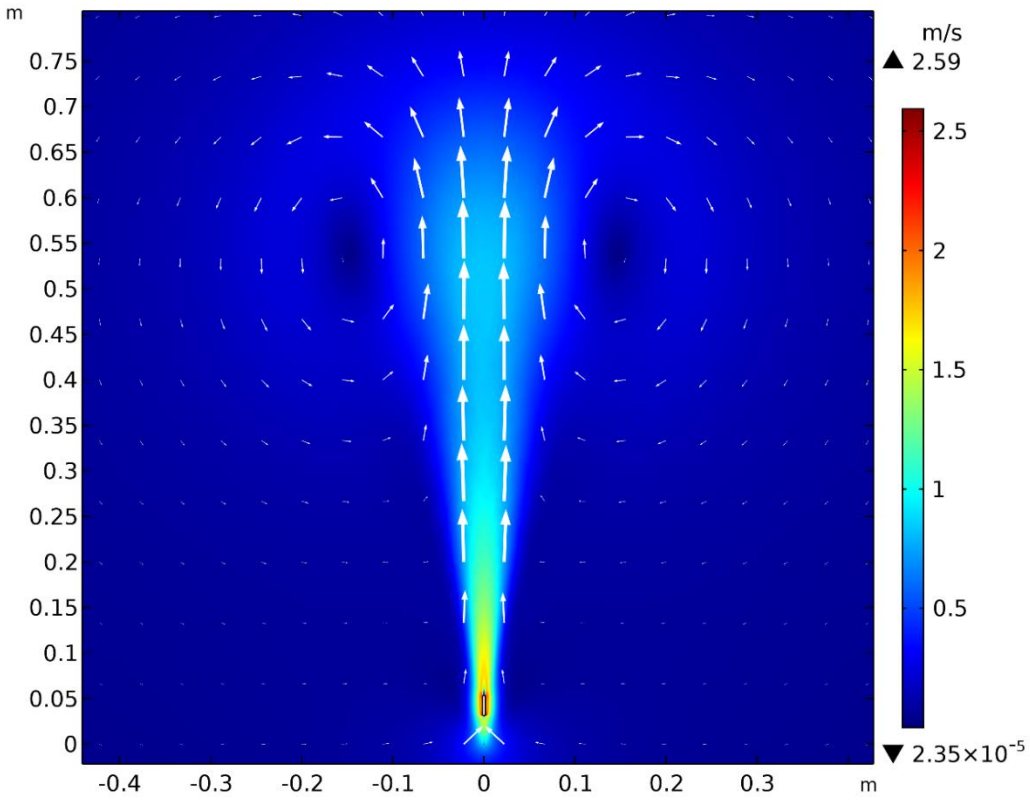

Fig. 12 Calculated velocity plot of air movement in m/s.

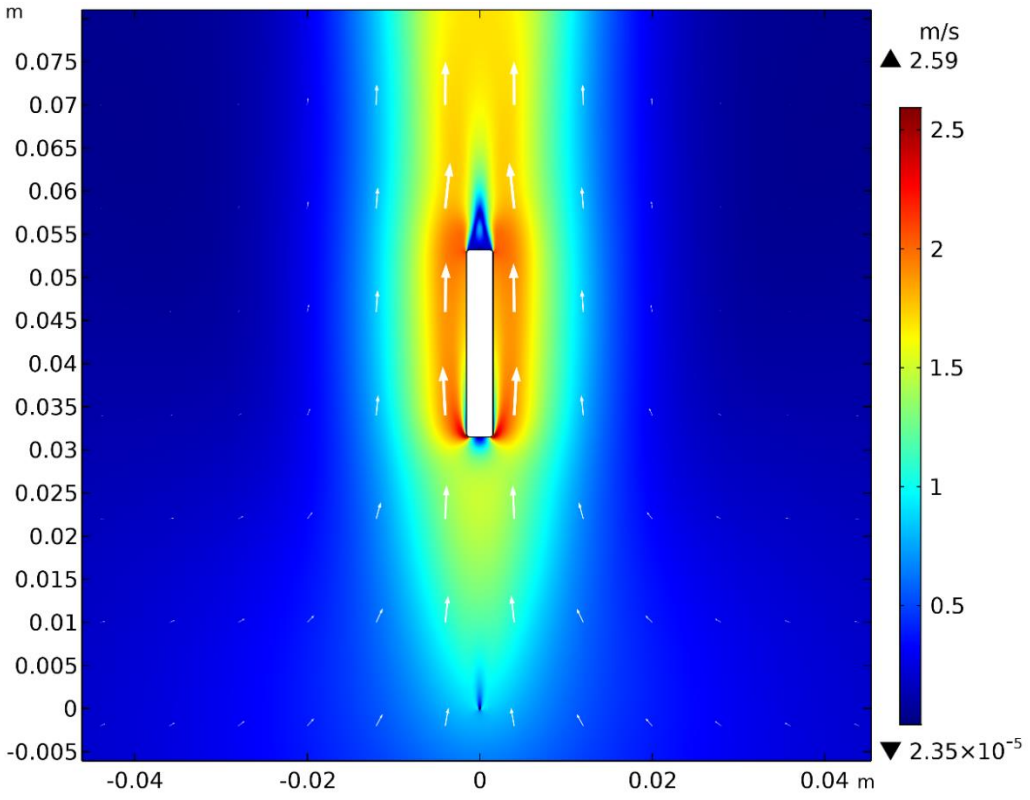

Fig. 13 Calculated velocity plot of air movement in m/s (magnification).

4.1.6 Volume force

The volume force in every node is calculated as a product of the space charge density and the vector of electric field strength. In Fig. 14 (left) the direction and the magnitude of the volume force vector field are depicted by the red arrows. The red arrows are mainly directed towards the large electrode. The thrust generated by the system is the integral of a vertical component of the volume force. From Fig. 14 (right) one can deduce that a very large volume force is generated close to the anode, but it is almost symmetrical. So, it does not contribute to the thrust, but consumes energy.

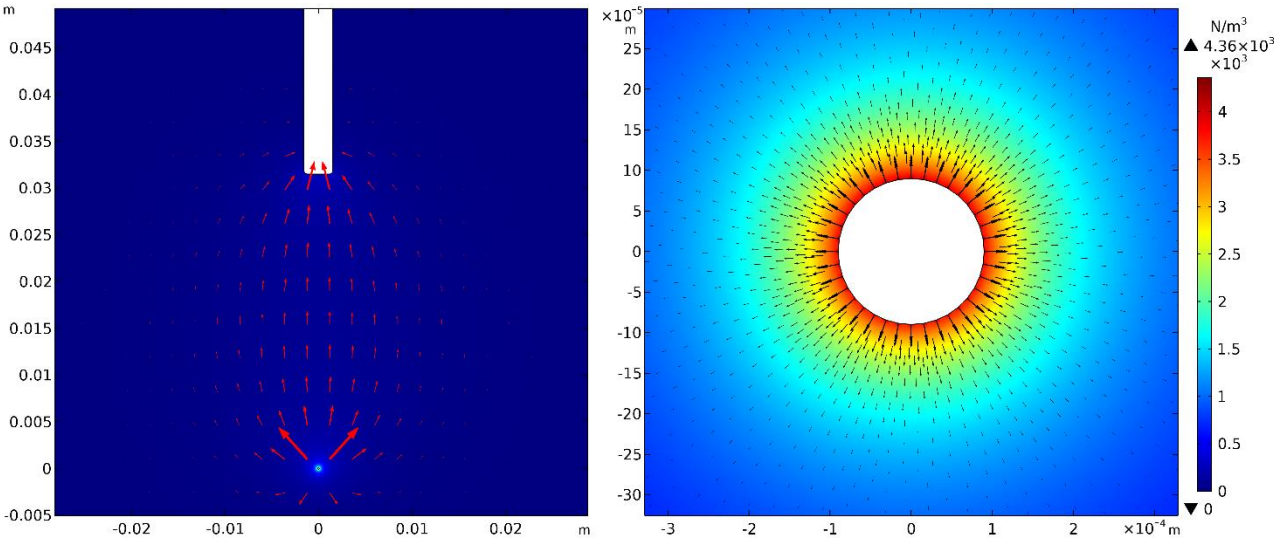

Fig. 14 Calculated volume force (left) and magnified volume force near the anode (right) in N/m^3.

4.2 Experimental results

As previously mentioned, the experimental investigation is divided into three parts: comparing different metals for the anode material, investigating the inter-electrode distance influence on the performance, and comparing the performance of systems with anodes of different diameters.

4.2.1 Metal comparison

Three different metal wires (tin, copper, brass) were used as anodes to identify the metal influence on the produced thrust. In all three tests, the inter-electrode distance was kept 31.5 mm. The diameters slightly varied as 0.47 mm, 0.48 mm, and 0.52 mm for brass, tin and copper respectively, as it was impossible to find identical wires.

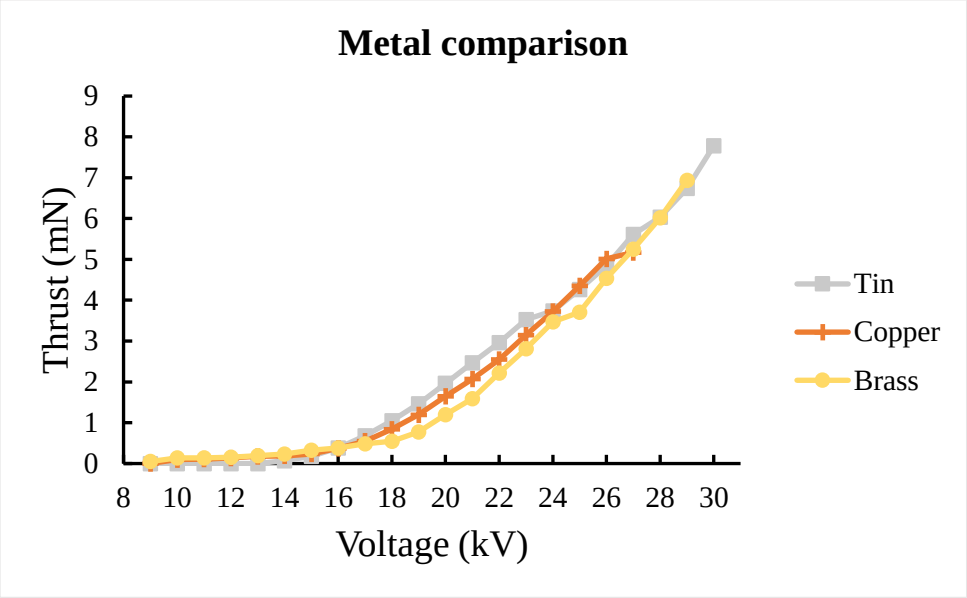

Fig. 16 Thrust characteristics of different metals.

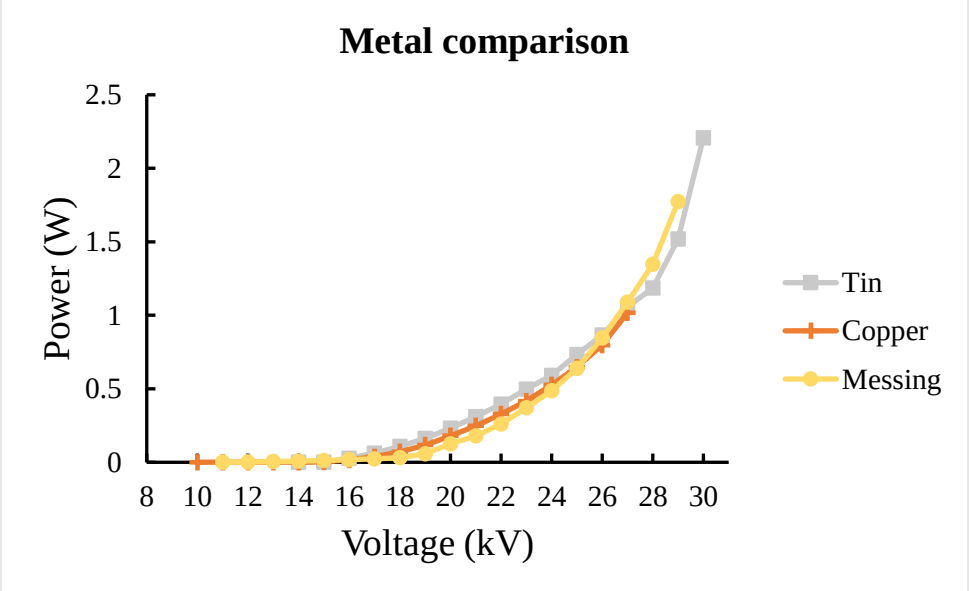

Fig. 15 Consumed power dependence on voltage for different metals in W.

It was assumed that such a small difference in diameter does not significantly influence the system's behavior, and if any important effect is associated with the type of metal, it would be visible. As depicted in Fig. 16, Fig. 15, and Fig. 17, the type of the anode metal does not

significantly influence the thrust, power, and thrust power efficiency characteristics. The difference in diameter can explain the small existing variations in thrust. The only important fact to mention is that more conductive metals initiate breakdown at smaller voltages than less conductive ones.

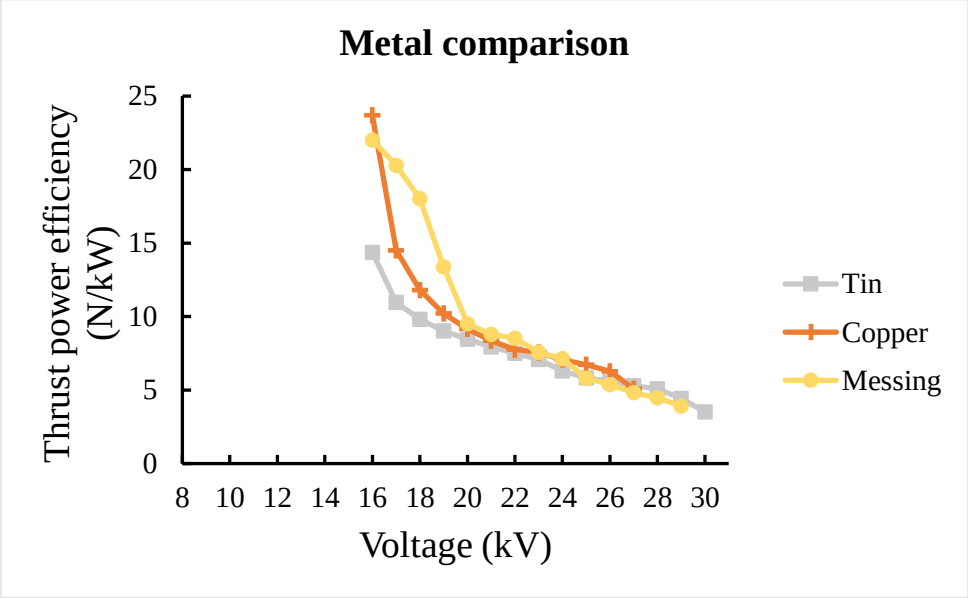

Fig. 17 Thrust power efficiency dependence on voltage for different metals in N/kW.

4.2.2 Diameter of the electrodes

The diameter of electrodes influences the thrust and power consumption more than the type of metal. The thrust voltage dependence can be observed in Fig. 18. Depending on the electrode

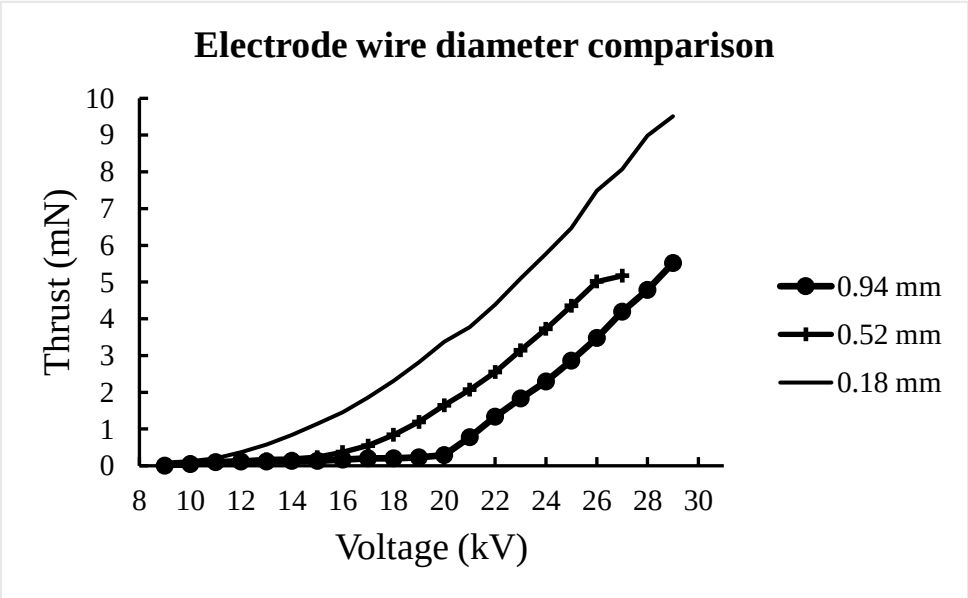

Fig. 18 Thrust dependence from voltage for wires with different diameters.

diameter, corona discharge starts at different voltages due to the local electric field enhancement on the electrodes with a smaller radius. It is evident that systems that generate more thrust consume more power, as shown in Fig. 19 depicting the power consumption. The thrust power

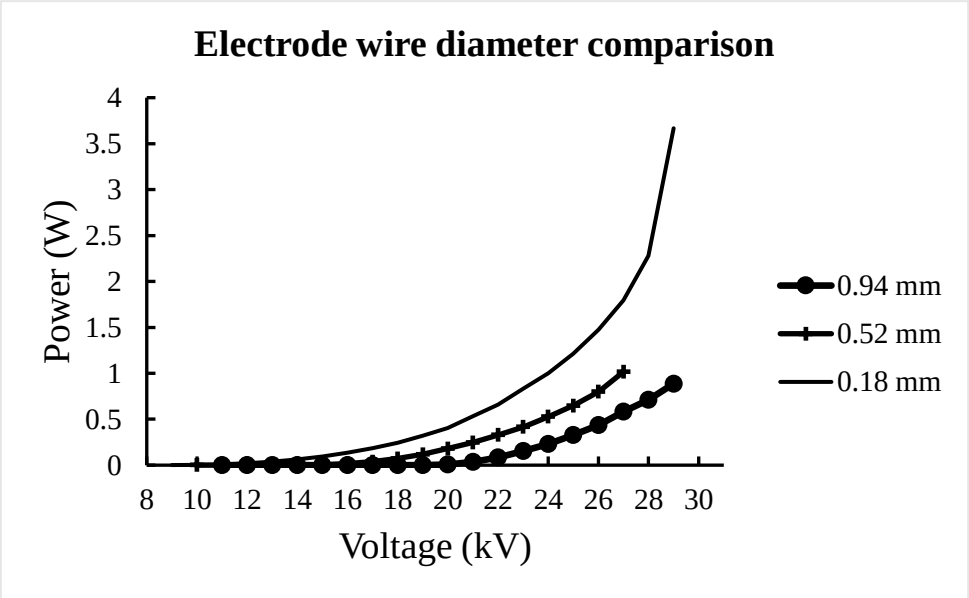

Fig. 19 Power dependence from voltage for wires with different diameters.

efficiency in the regime with a considerable thrust is approximately 10 N/kW, which corresponds to the existing literature [1]. Thrust efficiency is slightly better for larger electrodes, which is explained by the fact that larger electrodes generate smaller local electric field around the emitting electrode (anode). As we have seen in Fig. 14, the volume force around the anode is quite symmetrical. Therefore, the increase in field strength speeds up the ionization

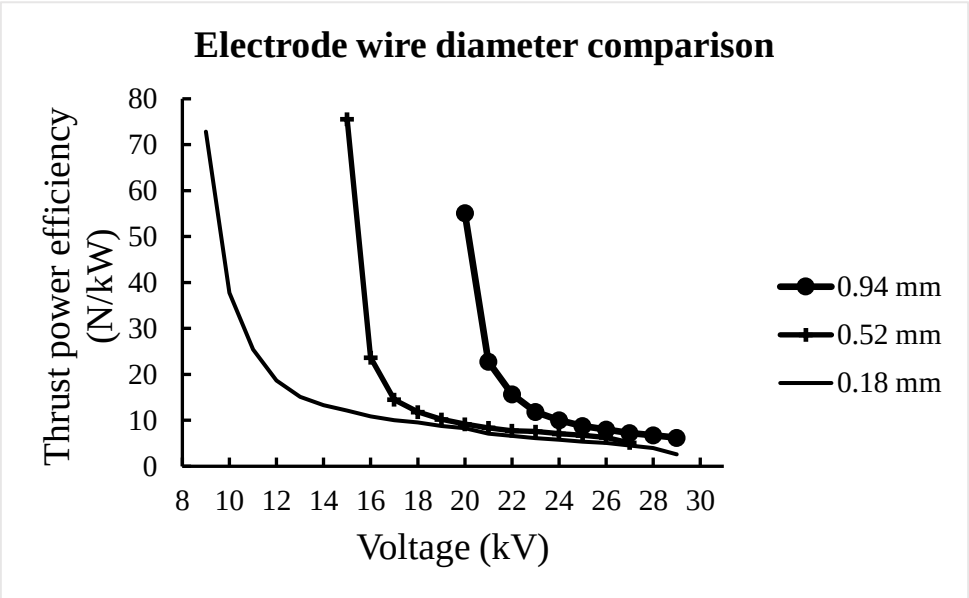

Fig. 20 Thrust power efficiency dependence from voltage for wires with different diameters.

rates and increases the charge densities, but simultaneously generates more significant symmetrical thrust from the anode. As symmetrical thrust does not contribute to the overall thrust, it is considered as energy loss.

4.2.3 Inter-electrode distance comparison

The brass electrode with 0.47 mm diameter was used to determine how inter-electrode distance influences the thrust and power characteristics. Fig. 21 represents thrust voltage dependencies for different inter-electrode distances. First of all, when voltage is being increased, breakdowns occur earlier for small inter-electrode distances. Thrust voltage dependence is sharper for smaller distances. Considering both effects, it is more reasonable to use intermediate inter-electrode distances to avoid breakdowns and have a sufficiently sharp thrust voltage curve. The distance of 31.5 mm was the most appropriate for the particular geometry of the experimental setup. A larger thrust requires a more powerful power supply. The power consumption is depicted in Fig. 22. Also, from the given figures, it is possible to approximately determine the starting voltage for the corona discharge. Fig. 23 shows that thrust power efficiency is very low for the distance of 16.5 mm, although for 31.5 mm and 51 mm, it is similar in the region of sufficient thrust (20kV-30kV).

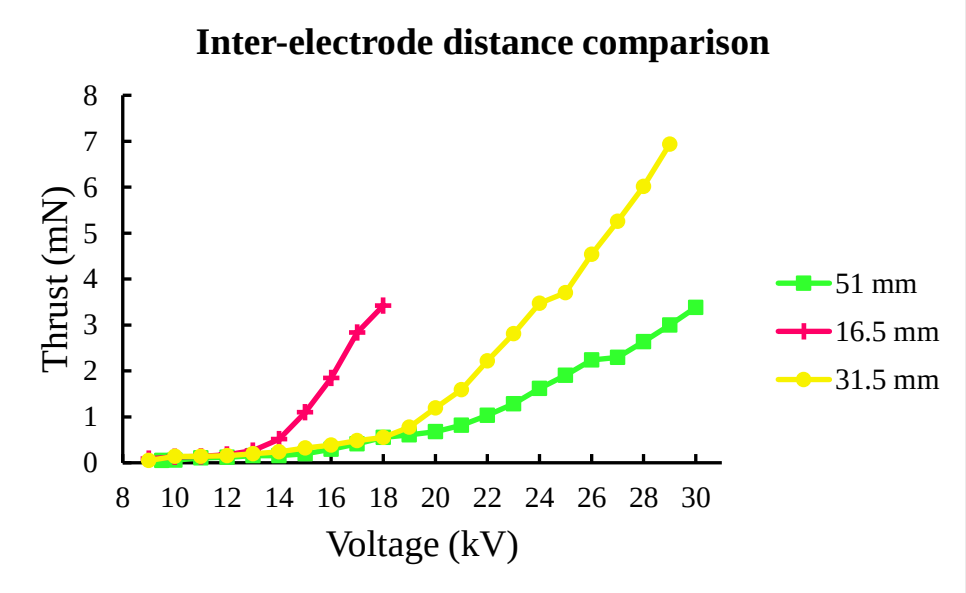

Fig. 21 Thrust voltage dependence for different inter-electrode distances.

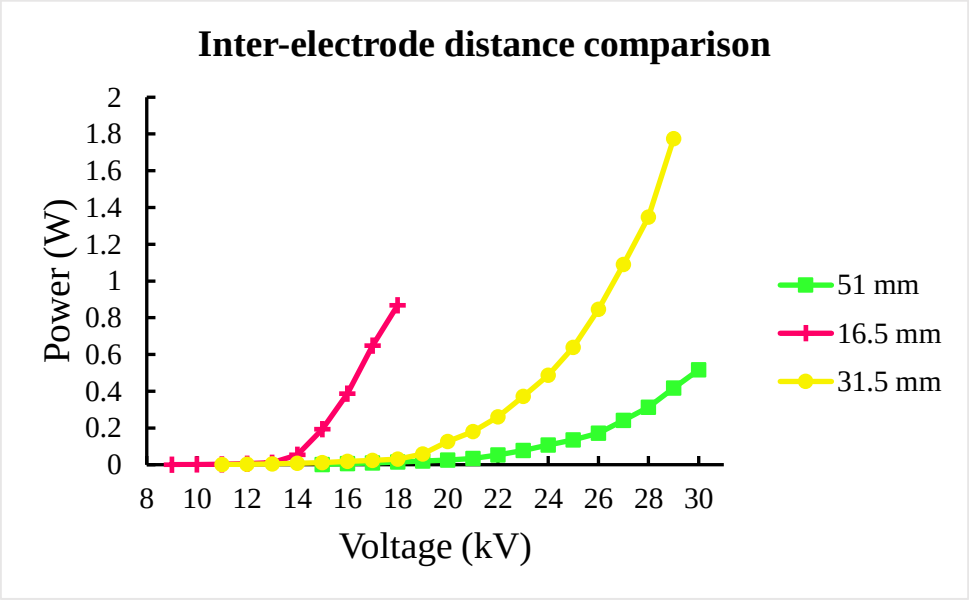

Fig. 22 Power voltage dependence for different inter-electrode distances.

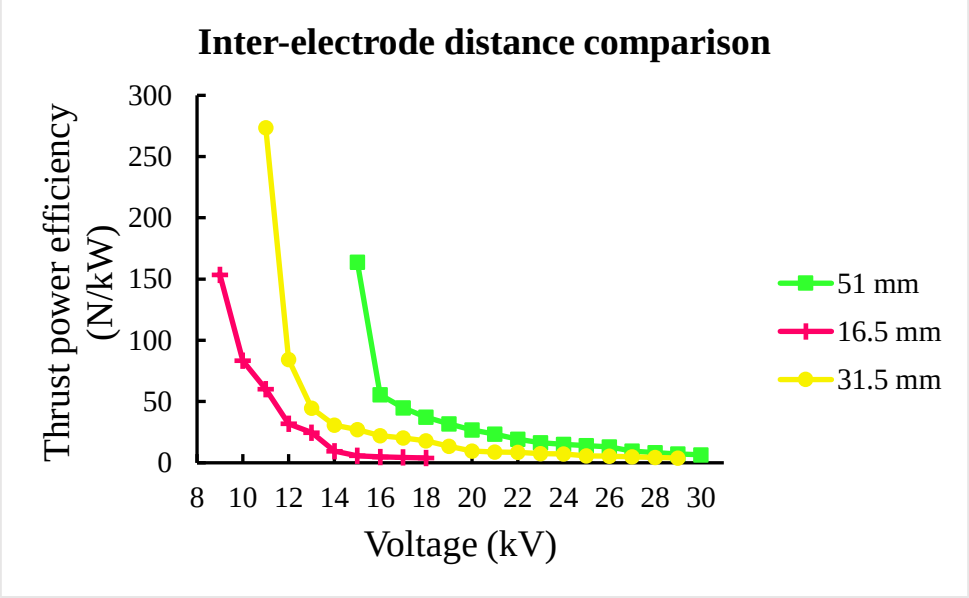

Fig. 23 Thrust power efficiency voltage dependence for different inter-electrode distances.

4.2.4 The optimal tradeoff between thrust and efficiency

It was analyzed that increasing the voltage, there is an increase in thrust, but the decrease in thrust power efficiency. So, there should be a particular voltage with simultaneously large enough efficiency and thrust. A thrust efficiency product was proposed for the estimation of thrust and efficiency at the same time. No units are used for that product as it would not have any physical meaning. One can depict from Fig. 24 that for many electrodes, the most productive voltage is 26 kV. At the same time, the curve of the most promising electrode configuration is marked by magenta markers. It is a copper electrode with a diameter of 0.18 mm and an inter-electrode distance of 31.5 mm. Graphs of the other electrodes are not so distinguishable from each other. This was done to emphasize the difference between the most promising electrode and the others. However, in every graph, we can see a local maximum with a smaller value than the absolute one. It suggests the change of the mechanism of corona discharge and has to be studied in more detail.

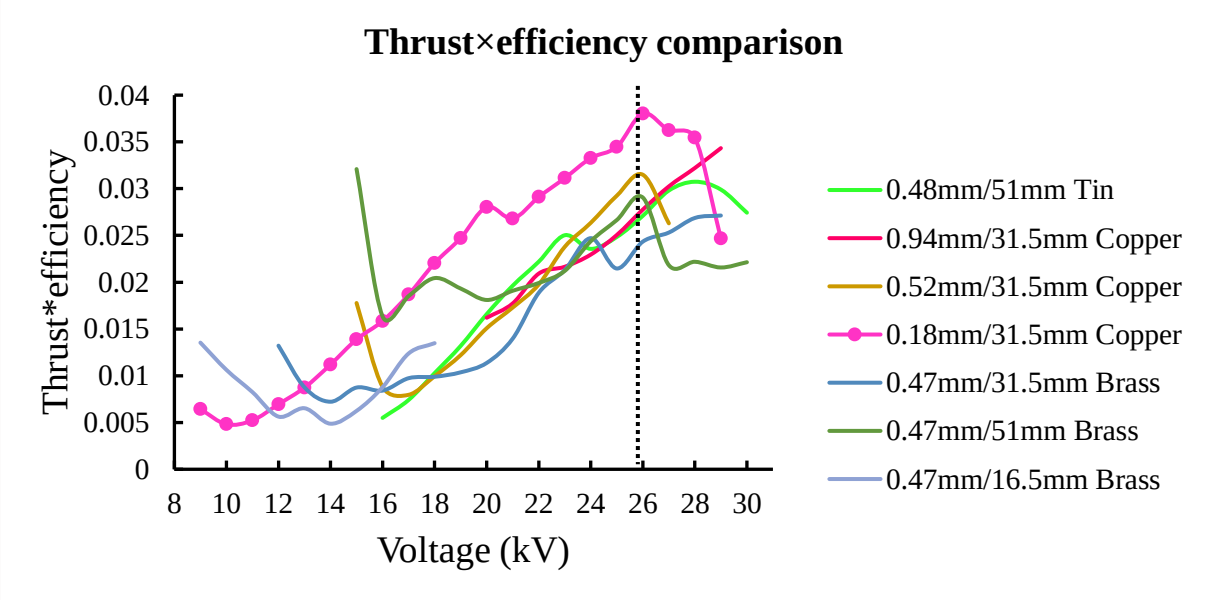

Fig. 24 Thrust efficiency product dependence on voltage for different electrodes.

4.3 Physical model validity

To compare simulation and experimental results in this thesis, the most efficient configuration described in the previous chapter was chosen. Other electrode configurations were also compared, but the results were almost identical. Therefore, these are not represented here.

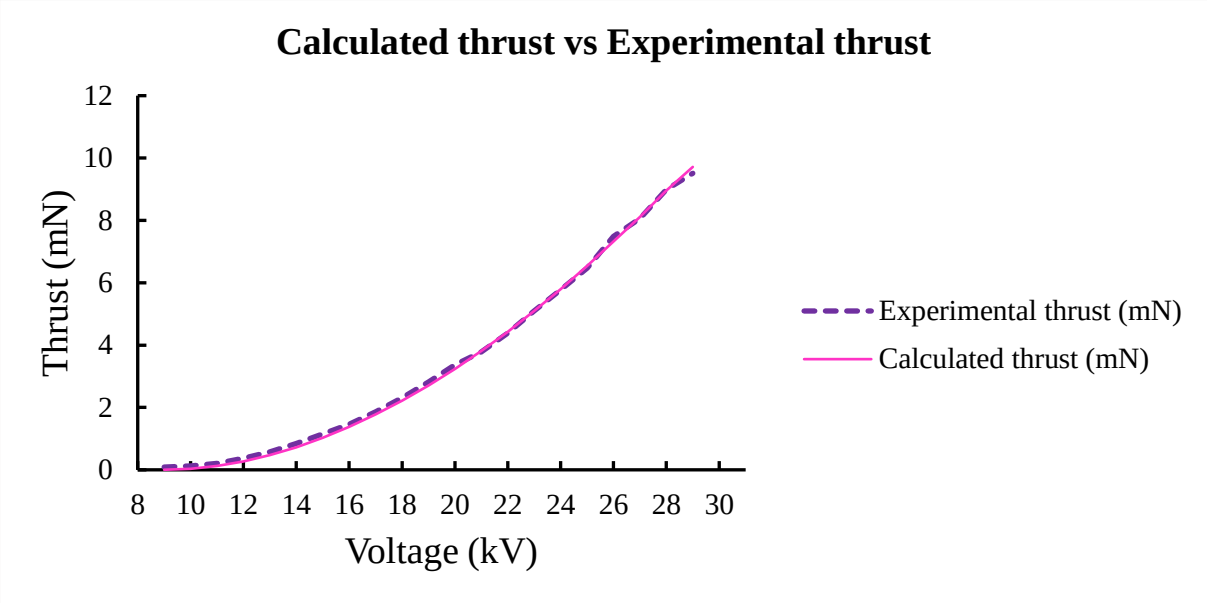

Fig. 25 The comparison of experimental thrust results with simulation.

In Fig. 25, the dashed line represents the thrust results obtained from the experiment, and the continuous line represents the thrust results from the simulation. The simulation model can be considered sufficiently precise as in the most crucial region for thruster application (19-29 kV), the average difference between experimental and simulation results was 1.5%. At the same time, the average percent deviation from the mean in experimental results was 3.2%. Therefore, it can be concluded that experimental and simulation methodology was chosen correctly, and the model is suitable for further development. The velocity measurements were also taken by the hot wire anemometer. The results were very similar to the simulation, but no precise measurements were taken. Precise velocity measurements will be conducted for validation of the next models.

5 Conclusions and outlook

5.1 Conclusions

The objectives of this work to increase the understanding of Biefeld-Brown effect and clarify the origin of the generated force, as well as to gain insight into the safety of the effect, were fulfilled. The force in the Biefeld-Brown effect comes from the transfer of potential energy of electric field into kinetic energy of ionized air molecules and the consequent momentum transfer to neutral molecules by a collision mechanism. The Biefeld-Brown effect can be considered environmentally friendly, but as high voltages are required for corona discharge generation, common high voltage safety requirements should be fulfilled.

A finite element method model simulating the Biefeld-Brown effect was developed utilizing the software package for equation-based multiphysics modeling COMSOL Multiphysics. Velocity, pressure, space charge density, potential, electric field strength, and volume force distributions were calculated, and the thrust was evaluated.

An experimental setup was created. It was concluded that different metals do not significantly influence the effect. Though, electrodes with higher conductivity favor breakdowns at smaller voltages applied. Electrodes with small diameters are more useful for generating thrust as their thrust×efficiency product is higher. Moderate inter-electrode distances are recommended for use because small inter-electrode distances favor early breakdowns, and too small thrusts are generated with large inter-electrode distances.

The simulation model was successfully validated. In the region of interest (19-29 kV), the average difference between experimental and simulation results was 1.5%.

The steps for the future research will be proposed in the following chapter.

5.2 Outlook and future research

Several steps are proposed for future research.

- Create a 3D drag evaluation model of an Ahmed body [38] and couple it with the existing thrust simulations of the BB effect for drag reduction calculations.
- Validate the numerical model with a drag experiment in a wind tunnel.
- Research possibilities for miniaturizing the electrodes.

- Research the possibilities to optimize the positioning and real-time operation of multiple BB thrusters on a vehicle, taking advantage of their electric controllability.
- Confirm observations that the employment of permanent magnets can influence the efficiency of the Biefeld-Brown effect [10].
- Introduce magnetic fields into the Ahmed body drag reduction simulations.
- Find the most effective positioning of electrodes and magnets on the surface.
- Validate simulation results with experiment. Conduct drag tests of Ahmed body in a wind tunnel with different positioning of electrodes and magnets on its surface.

Successful fulfillment of these objectives would fill the gap between the current state of the art and the desired future.

Acknowledgments

First of all, I would like to sincerely thank Alvo Aabloo, Andreas Kyritsakis and Vahur Zadin for being great supervisors and providing essential insights for my bachelor thesis. It was especially valuable to learn by comparing technics and suggestions received simultaneously from three profound scientists.

I thank Vahur Zadin for significantly easing my learning curve of COMSOL Multiphysics and for important comments on how to approach different technical challenges.

I am very grateful to Andreas Kyritsakis for fruitful discussions, sometimes long hours, on various phenomena, which gradually enhanced my physical intuition.

I would like to thank Alvo Aabloo for creating all the necessary conditions for efficient work and studies, as well as exciting talks that boosted my imagination.

Additionally, I thank Indrek Must for demonstrating to me that a simple experimental setup can be made in minutes and using handy materials and Indrek Jõgi for providing safety instructions for working with high voltage.

Last but not least, I express my deepest gratitude to Hana for supporting me throughout my work and sharing my excitement in science and life.

References

[1] J. Wilson, H. D. Perkins, and W. K. Thompson, ‘An Investigation of Ionic Wind Propulsion’, p. 43, 2009.

[2] L. Leger, E. Moreau, and G. G. Touchard, ‘Effect of a DC corona electrical discharge on the airflow along a flat plate’, *IEEE Trans. on Ind. Applicat.*, vol. 38, no. 6, pp. 1478–1485, Nov. 2002, doi: 10.1109/TIA.2002.804769.

[3] E. Moreau, L. Léger, and G. Touchard, ‘Effect of a DC surface-corona discharge on a flat plate boundary layer for air flow velocity up to 25m/s’, *Journal of Electrostatics*, vol. 64, no. 3–4, pp. 215–225, Mar. 2006, doi: 10.1016/j.elstat.2005.05.009.

[4] K. Zhou, G. Ding, Y. Wang, and J. Niu, ‘Aeroheating and aerodynamic performance of a transonic hyperloop pod with radial gap and axial channel: A contrastive study’, *Journal of Wind Engineering and Industrial Aerodynamics*, vol. 212, p. 104591, May 2021, doi: 10.1016/j.jweia.2021.104591.

[5] J. M. Mateu, P. Martínez Fernández, and R. Insa Franco, ‘Setting safety foundations in the Hyperloop: A first approach to preliminary hazard analysis and safety assurance system’, *Safety Science*, vol. 142, p. 105366, Oct. 2021, doi: 10.1016/j.ssci.2021.105366.

[6] M. M. Wojewodka, C. White, and K. Kontis, ‘Effect of permittivity and frequency on induced velocity in ac-DBD surface and channel plasma actuators’, *Sensors and Actuators A: Physical*, vol. 303, p. 111831, Mar. 2020, doi: 10.1016/j.sna.2020.111831.

[7] A. Tang, R. S. Vaddi, A. Mamishev, and I. V. Novosselov, ‘Empirical relations for discharge current and momentum injection in dielectric barrier discharge plasma actuators’, *J. Phys. D: Appl. Phys.*, vol. 54, no. 24, p. 245204, Jun. 2021, doi: 10.1088/1361-6463/abec0b.

[8] F. Rodrigues, A. Mushyam, J. Pascoa, and M. Trancossi, ‘A new plasma actuator configuration for improved efficiency: the stair-shaped dielectric barrier discharge actuator’, *J. Phys. D: Appl. Phys.*, vol. 52, no. 38, p. 385201, Sep. 2019, doi: 10.1088/1361-6463/ab2584.

[9] Y. Li *et al.*, ‘Turbulent boundary layer control with a spanwise array of DBD plasma actuators’, *Plasma Sci. Technol.*, vol. 23, no. 2, p. 025501, Feb. 2021, doi: 10.1088/2058-6272/abce0d.

[10] G. Matsoukas and N. Ahmed, ‘Experimental Investigation of Asymmetrical Capacitors for Electric Propulsion’, Sep. 2014, pp. 2014-01–2221. doi: 10.4271/2014-01-2221.

[11] *COMSOL Multiphysics® v. 5.5*. COMSOL AB, Stockholm, Sweden. [Online]. Available: www.comsol.com

[12] N. Cabeo, *Philosophia Magnetica*. Cologne, Germany: Francesco Suzzi, Ferrara, 1629.

[13] F. Hauksbee, *Physico-mechanical Experiments on Various Subjects*. 1709.

[14] T. Townsend Brown, ‘Electrokinetic Apparatus’, Jul. 03, 1957

[15] H. Fantel, ‘Major De Seversky’s Ion-Propelled Aircraft’, 1964.

[16] S.-I. Cheng, ‘Glow Discharge as an Advanced Propulsion Device’, *ARS Journal*, vol. 32, no. 12, pp. 1910–1916, Dec. 1962, doi: 10.2514/8.6422.

[17] E. A. Christenson and P. S. Moller, ‘Ion-neutral propulsion in atmospheric media.’, *AIAA Journal*, vol. 5, no. 10, pp. 1768–1773, Oct. 1967, doi: 10.2514/3.4302.

[18] M. Robinson, ‘Movement of Air in the Electric Wind of the Corona Discharge’, p. 8, 1961.

[19] H. Bondar and F. Bastien, ‘Effect of neutral fluid velocity on direct conversion from electrical to fluid kinetic energy in an electro-fluid-dynamics (EFD) device’, *J. Phys. D: Appl. Phys.*, vol. 19, no. 9, pp. 1657–1663, Sep. 1986, doi: 10.1088/0022-3727/19/9/011.

[20] R. Talley, ‘Twenty First Century Propulsion Concept’. 1988.

[21] L. Pekker and M. Young, ‘Model of Ideal Electrohydrodynamic Thruster’, *Journal of Propulsion and Power*, vol. 27, no. 4, pp. 786–792, Jul. 2011, doi: 10.2514/1.B34097.

[22] F. X. Canning, C. Melcher, and E. Winet, ‘Asymmetrical Capacitors for Propulsion’, p. 23, 2004.

[23] G. Matsoukas and N. A. Ahmed, ‘Experimental investigation of employing asymmetrical electrodes in propulsion of vehicles’, *Procedia Engineering*, p. 7, 2012.

[24] N. E. Jewell-Larsen, S. V. Karpov, I. A. Krichtafovitch, V. Jayanty, C.-P. Hsu, and A. V. Mamishev, ‘Modeling of corona-induced electrohydrodynamic flow with COMSOL multiphysics’, p. 13, 2008.

[25] P. Mikropoulos and V. Zagkanas, ‘Threshold inception conditions for positive DC corona in the coaxial cylindrical electrode arrangement under variable atmospheric conditions’, *IEEE Trans. Dielect. Electr. Insul.*, vol. 22, no. 1, pp. 278–286, Feb. 2015, doi: 10.1109/TDEI.2014.004641.

[26] M. Einat and R. Kalderon, ‘High efficiency Lifter based on the Biefeld-Brown effect’, *AIP Advances*, vol. 4, no. 7, p. 077120, Jul. 2014, doi: 10.1063/1.4890353.

[27] G. Hartmann, ‘Theoretical Evaluation of Peek’s Law’, *IEEE Trans. on Ind. Applicat.*, vol. IA-20, no. 6, pp. 1647–1651, Nov. 1984, doi: 10.1109/TIA.1984.4504655.

[28] J. D. McClurkin, D. E. Maier, and K. E. Ileleji, ‘Half-life time of ozone as a function of air movement and conditions in a sealed container’, *Journal of Stored Products Research*, vol. 55, pp. 41–47, Oct. 2013, doi: 10.1016/j.jspr.2013.07.006.

[29] S. Pancheshnyi, ‘Effective ionization rate in nitrogen–oxygen mixtures’, *J. Phys. D: Appl. Phys.*, vol. 46, no. 15, p. 155201, Apr. 2013, doi: 10.1088/0022-3727/46/15/155201.

[30] P. O. Bedolla, G. Vorlaufer, P. Sequard-Base, A. Vernes, and F. Franek, ‘Altitude dependence of electrohydrodynamic flow in an electrostatic lifter’, *Journal of Electrostatics*, vol. 87, pp. 32–44, Jun. 2017, doi: 10.1016/j.elstat.2017.03.003.

[31] B. Rehm, D. Consultant, A. Haghshenas, A. S. Paknejad, and J. Schubert, ‘Situational Problems in MPD’, in *Managed Pressure Drilling*, Elsevier, 2008, pp. 39–80. doi: 10.1016/B978-1-933762-24-1.50008-5.

[32] *CFD Module User’s Guide*. COMSOL AB, Stockholm, Sweden: COMSOL Multiphysics®, 2019.

[33] D. McLean, *Understanding aerodynamics: arguing from the real physics*. Chichester, West Sussex, United Kingdom: Wiley, 2013.

[34] Eimre, Kristjan, ‘Implementing the general thermal-field emission equation to the high electric field nanoprotrusion model’.

[35] O. C. Zienkiewicz, R. L. Taylor, and J. Z. Zhu, *The finite element method: its basis and fundamentals*, 6. ed., Reprint., Transferred to digital print. Amsterdam Heidelberg: Elsevier, 2010.

[36] G. R. Liu and S. S. Quek, 'Computational Modeling', in *The Finite Element Method*, Elsevier, 2014, pp. 1–11. doi: 10.1016/B978-0-08-098356-1.00001-1.

[37] E. Moreau, N. Benard, F. Alicalapa, and A. Douyère, 'Electrohydrodynamic force produced by a corona discharge between a wire active electrode and several cylinder electrodes – Application to electric propulsion', *Journal of Electrostatics*, vol. 76, pp. 194–200, Aug. 2015, doi: 10.1016/j.elstat.2015.05.025.

[38] T. Hughes, 'CFD Study of Flow over a Simplified Car (Ahmed Body) Using Different Turbulence Models', May 2018.

Appendix

Less, though still important figures of the thesis are placed in the appendix for more interested readers to familiarise themselves.

Mesh figures

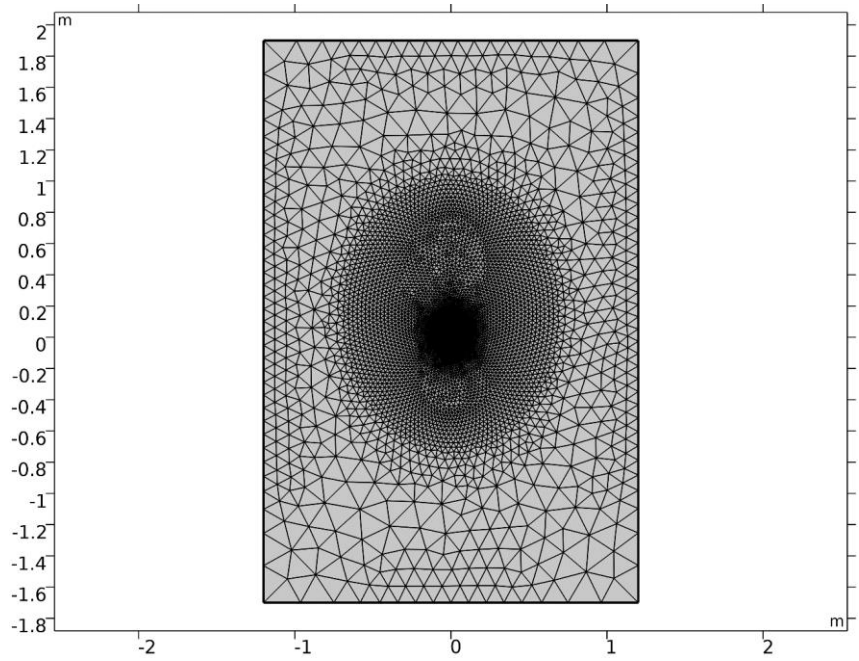

Fig. 26 Mesh of simulated system.

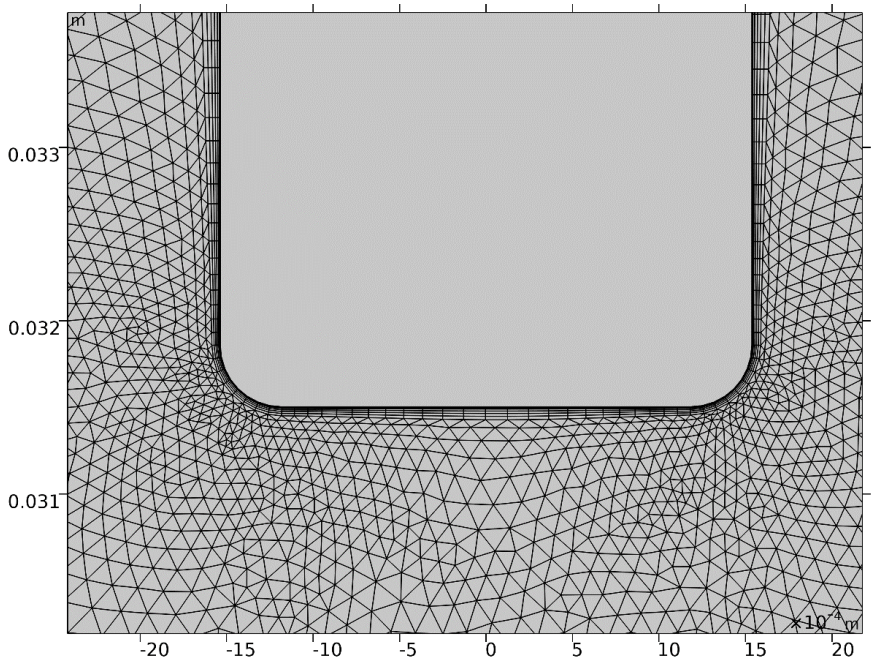

Fig. 27 Bottom side of aluminum cathode.

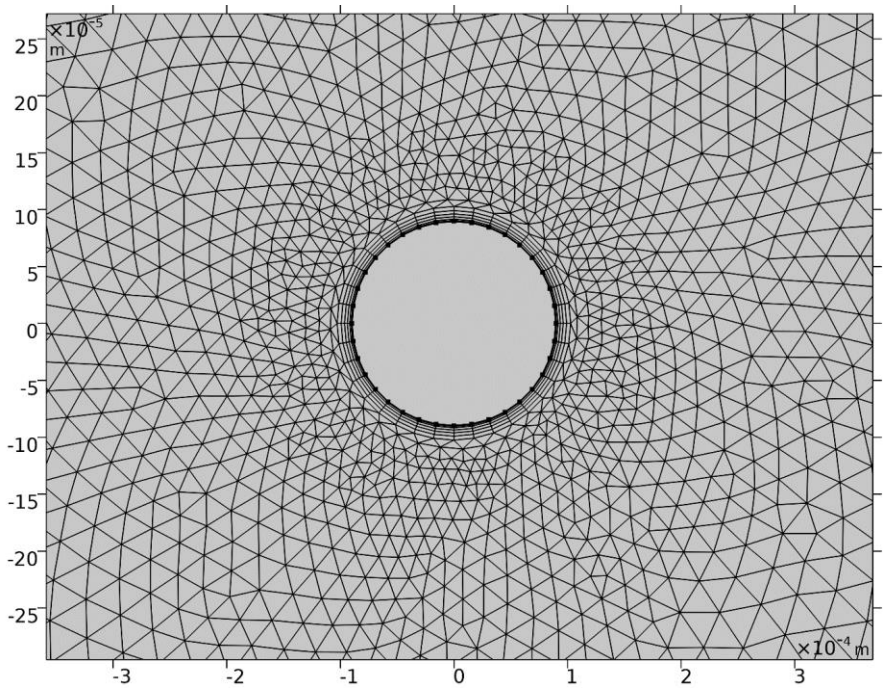

Fig. 28 Mesh of the positive copper anode.

Figures of the simulation results

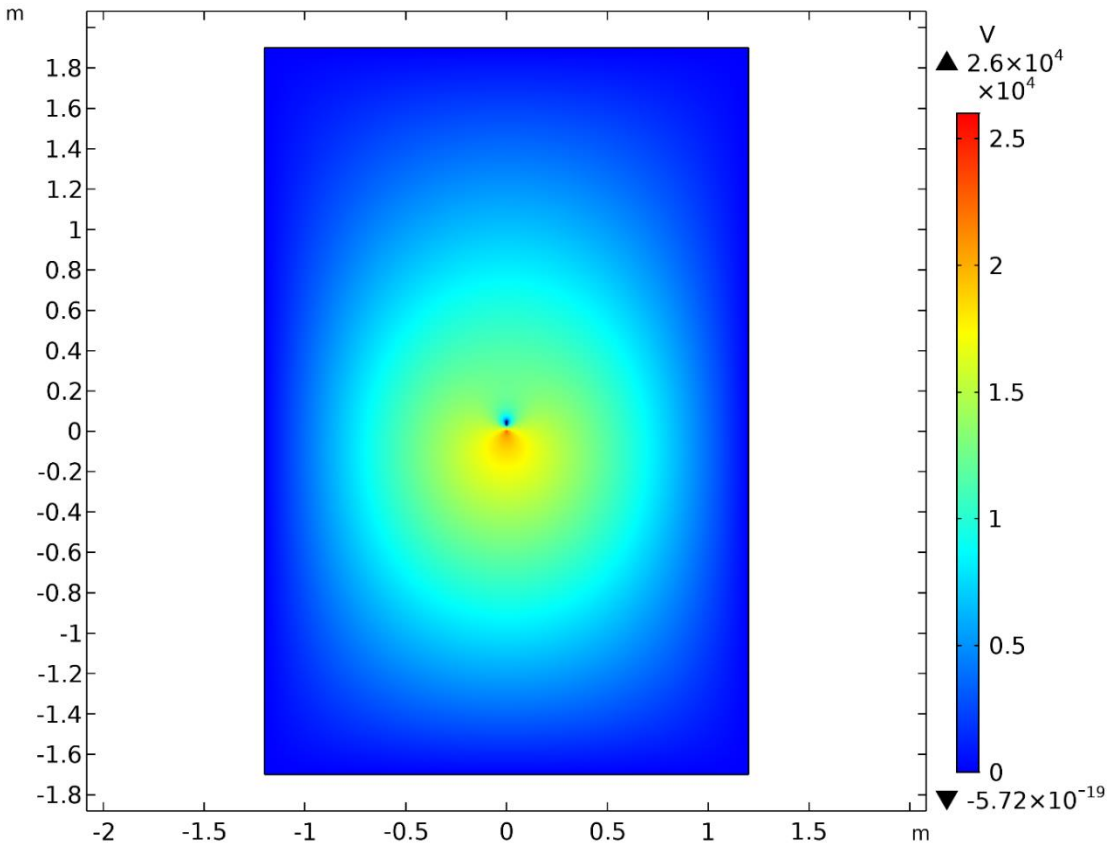

Fig. 29 Electric potential in V.

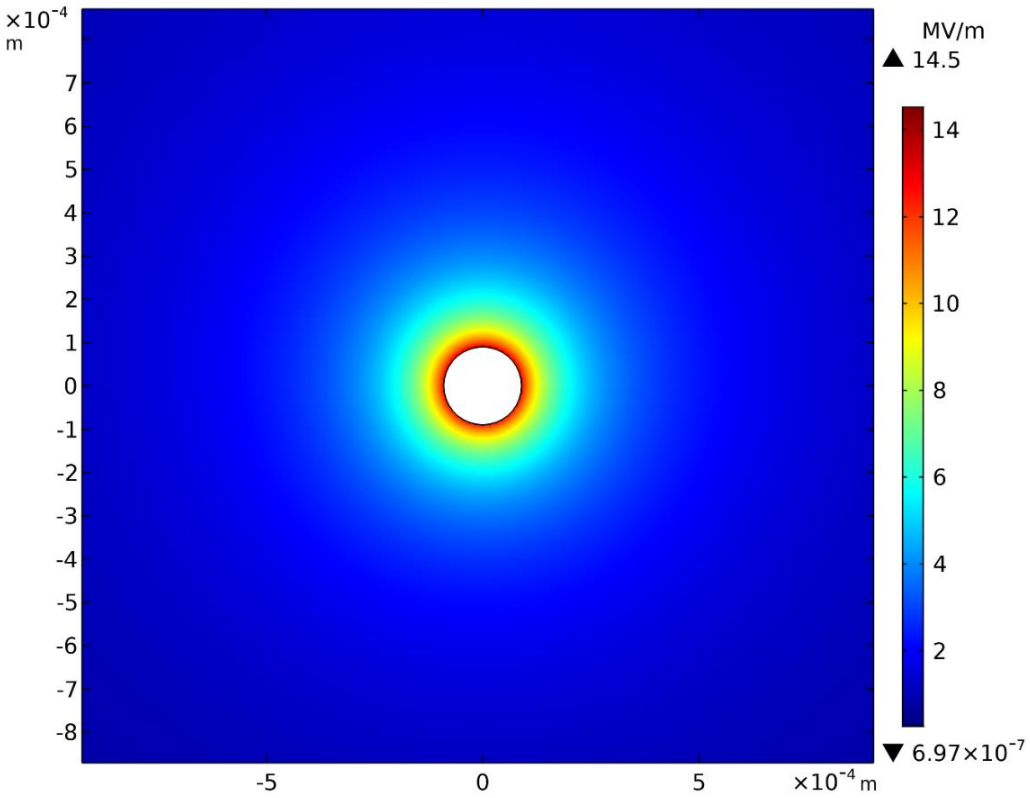

Fig. 30 Calculated electric field close to the anode in MV/m.

Non-exclusive licence to reproduce thesis and make thesis public

I, Juri Volodin

1. herewith grant the University of Tartu a free permit (non-exclusive licence) to:

1.1. reproduce, for the purpose of preservation, including for adding to the DSpace digital archives until the expiry of the term of copyright, and

1.2. make available to the public via the web environment of the University of Tartu, including via the DSpace digital archives, under the Creative Commons licence CC BY NC ND 3.0, which allows, by giving appropriate credit to the author, to reproduce, distribute the work and communicate it to the public, and prohibits the creation of derivative works and any commercial use of the work from ***01/08/2024*** until the expiry of the term of copyright,

Modeling and experimental study of the Biefeld-Brown effect,

supervised by Alvo Aabloo, Andreas Kyritsakis, Vahur Zadin.

2. I am aware of the fact that the author retains the rights specified in p. 1.

3. I certify that granting the non-exclusive licence does not infringe other persons' intellectual property rights or rights arising from the personal data protection legislation.

Juri Volodin

09/08/2021